

Megadunes in Antarctica: migration and characterization from remote and in situ observations

Giacomo Traversa^{1,2}, Davide Fugazza²Fugazza³ and Massimo Frezzotti³Frezzotti⁴

Formattato: SpazioPrima: 6 pt

¹[Institute of Polar Sciences, National Research Council of Italy, 20125 Milano, Italy](#)

ha formattato: Inglese (Stati Uniti)

²Department of Physical Sciences, Earth and Environment (DSFTA), Università degli Studi di Siena, 53100 Siena, Italy

Formattato: SpazioPrima: 0 pt

³Department of Environmental Science and Policy (ESP), Università degli Studi di Milano, 20133 Milan, Italy

ha formattato: Inglese (Stati Uniti)

⁴Department of Science, Università degli Studi Roma Tre, 00146 Rome, Italy

5

Correspondence to: Giacomo Traversa (giacomo.traversa@student.unisi.it) and Massimo Frezzotti (massimo.frezzotti@uniroma3.it)

Codice campo modificato

Abstract. Megadunes are peculiar features formed by the interaction between atmosphere and cryosphere and are known to be present only on the East Antarctic plateau and other planets (Mars and Pluto). In this study, we have analysed the glaciological dynamic of megadunes, their spectral properties and morphology on two sample areas of the East Antarctic plateau where in the past international field activities were carried out (EAIIST and It-ITASE). Using satellite images spanning 7 years, we analysed the spatial and temporal variability of megadune surface characteristics, i.e., near infrared (NIR) albedo, thermal brightness temperature (BT) and Slope along the Prevailing Wind Direction (SPWD), useful for mapping them. These parameters allowed us to characterise and perform an automated detection of the glazed surfaces, and we determined the influence of the SPWD by ~~including it and excluding it from the detection approach. The exclusion of the SPWD resulted in an 88% overestimation in the detection of glazed surfaces evaluating different combination of these parameters. The inclusion of the SPWD significantly increased the accuracy of the method, doubling it in certain analysed scenes.~~ Using remote and field observations, for the first time we surveyed all the components of upwind migration (absolute, sedimentological and ice flow), ~~with finding~~ an absolute value of about 10 m a^{-1} . The analysis shows that the migration is driven by the snow accumulation on the crest and through prograding upwind on the previous windward flanks characterised by glazed surface. Our results present significant implications for Surface Mass Balance estimation, paleoclimate reconstruction using ice cores and for the measurements using optical and radar images/data in the megadune ~~area~~areas.

1 Introduction

Antarctic climate and mass balance have been highlighted by the Special Report on the Ocean and Cryosphere in a Changing Climate (Meredith et al., 2019) by the Intergovernmental Panel on Climate Change (IPCC) among the main uncertainties for the climate system and sea level projections. Surface mass balance (SMB) is the net balance between the processes of snow precipitation and loss on a glacier surface and provides mass input to the surface of the Antarctic Ice Sheet. Therefore, it represents an important control on ice sheet mass balance and resulting contribution to global sea level change. Ice sheet SMB

varies greatly across multiple scales of time (hourly to decadal) and space (metres to hundreds of kilometres), and it is 35 notoriously challenging to observe and represent in atmospheric models (eg. Agosta et al., 2019; Lenaerts et al., 2019).

Moreover, given the difficulties in accessing the interior of the ice sheet, only limited field observation on past and current 40 conditions exists. The Southern part of the East Antarctic Ice Divide, from Concordia and Vostok Stations to the South Pole is the coldest and driest area on Earth and presents unique features called megadunes, which extend for more than 500,000 km² (Fahnestock et al., 2000). The drivers of megadune formation are uncommon snow accumulation and redistribution processes driven by wind scouring that remain relatively unexplained (Fahnestock et al., 2000; Frezzotti et al., 2002a, b; 45 Courville et al., 2007; Scambos et al., 2012; Dadic et al., 2013; Ekaykin et al., 2015, Fig. 1). Ground surveys of megadunes show that snow is removed from their leeward slopes where a specific erosional type of snow, “glazed surface” or “wind crust”, is formed as a result. In contrast, snow accumulation is increased on the windward slopes that are characterised by the depositional types of the snow microrelief termed “sastrugi”. Glazed surfaces form because wind and sublimation can ablate 50 much more snow/firn than is accumulated by annual solid precipitation, causing a persistent SMB close to zero or negative.

The stability of climatic conditions could play a key role in megadune formation, since aecumulationsnow precipitation is very 55 low while katabatic wind intensity and direction are stable; these conditions affect snow sintering and a high grade of snow metamorphism (Albert et al., 2004; Courville et al., 2007; Scambos et al., 2012; Dadic et al., 2013). Megadunes are oriented perpendicular to the Slope along the Prevailing Wind Direction (SPWD), wave amplitudes are small (up to 8 m), wavelengths 60 range from 2 to over 5 km and megadune crests are nearly parallel, extending from tens to hundreds of kilometres (Swithinbank, 1988; Fahnestock et al., 2000; Frezzotti et al., 2002a, b; Arcone et al., 2012a, b). The angle between the katabatic wind direction and the direction of general surface slope at a regional scale can differ up to 50° due to the interaction between the topographic slope driving gravity and the Coriolis force (Fahnestock et al., 2000; Frezzotti et al., 2002b).

Based on previous studies, the SMB of megadunes ranges between 25% (leeward faces glazed surfaces) and 120% (windward 65 faces, covered by huge sastrugi up to 1.5 m in height) of accumulation in adjacent non-megadune areas (Frezzotti et al., 2002b).

The sedimentary structure of buried megadunes examined via Ground Penetrating Radar (GPR) and Global Position System (GPS) suggests that the sedimentary morphology of the windward face (sastrugi) migrates upwind with time, burying the 70 glazed surface of the leeward face (Frezzotti et al., 2002b; Ekaykin et al., 2015), with typical “antidune” processes similar to those observed on fluvial and ocean bedforms (Prothero and Schwab, 2004). This uphill migration is caused by the difference in accumulation between windward (high accumulation) and leeward (near-zero or negative accumulation) sides, also leading 75 to differences in snow features and surface roughness (Fahnestock et al., 2000; Frezzotti et al., 2002a; Albert et al., 2004; Courville et al., 2007). Megadunes appear to be formed by an oscillation in the katabatic air flow, leading to a wave-like variation in net accumulation; the wind-waves are formed at the change of SPWD, in response to the buoyancy force, favouring the standing-wave mechanism (Fahnestock et al., 2000; Frezzotti et al., 2002b). According to Dadic et al. (2013), who based 80 his analysis on superficial-flow theory for sediments in water (Núñez-González and Martín-Vide, 2011) and atmospheric flow modelling, persistent katabatic winds, strong atmospheric stability and spatial variability in surface roughness are the primary 85

controllers of upwind accumulation and migration of megadunes, where the latter represents the main factor that influences their velocity.

The surface waveforms of megadunes with regular bands of sastrugi and glazed surfaces allow surveying the megadunes by 70 satellite observations, because of differences in albedo and microwave backscatter (Fahnestock et al., 2000; Frezzotti et al., 2002a; Scambos et al., 2012) between these features and surrounding snow. Spectral differences also lead to an effect on temperatures, which is on average higher than on the snow surface (Fujii et al., 1987). In spite of the importance of the glazed surfaces of megadunes for the SMB of Antarctica, a remote sensing characterization of their physical properties and spatial distribution, and a quantitative analysis of their migration is currently lacking. The aim of the study is to provide a detailed 75 survey of the spatial and temporal variability of two megadune areas using remote sensing data (Landsat 8 and Sentinel-2), high resolution elevation models (Reference Elevation Model of Antarctica REMA, Howat et al., 2019) and climatic conditions using atmospheric reanalysis data (ERA5) in addition to past in-situ measurement data (firn core, GPR and GPS), to explore spectral, thermal, and windward slope relationships with a view towards generating an algorithm for their automatic detection. Moreover, we provide for the first time the first calculationmeasurements of the absolute megadune movement, and its different 80 components: ice-flow and sedimentological progradation. The analysis of absolute megadune movement has important implications on the remote sensing ice dynamic measurements, in particular on ice flow measurements and elevation changes. Our work constitutes substantial progress towards the survey of ablation areas on SMB at small spatial scales over ice sheets using surface morphology (SPWD) and albedo detection by satellite. A clear understanding of these interactions is of primary importance for the climatic interpretation of ice records and for the assessment of processes and rates of wind scouring and its 85 SMB implications.

1.1 Study area

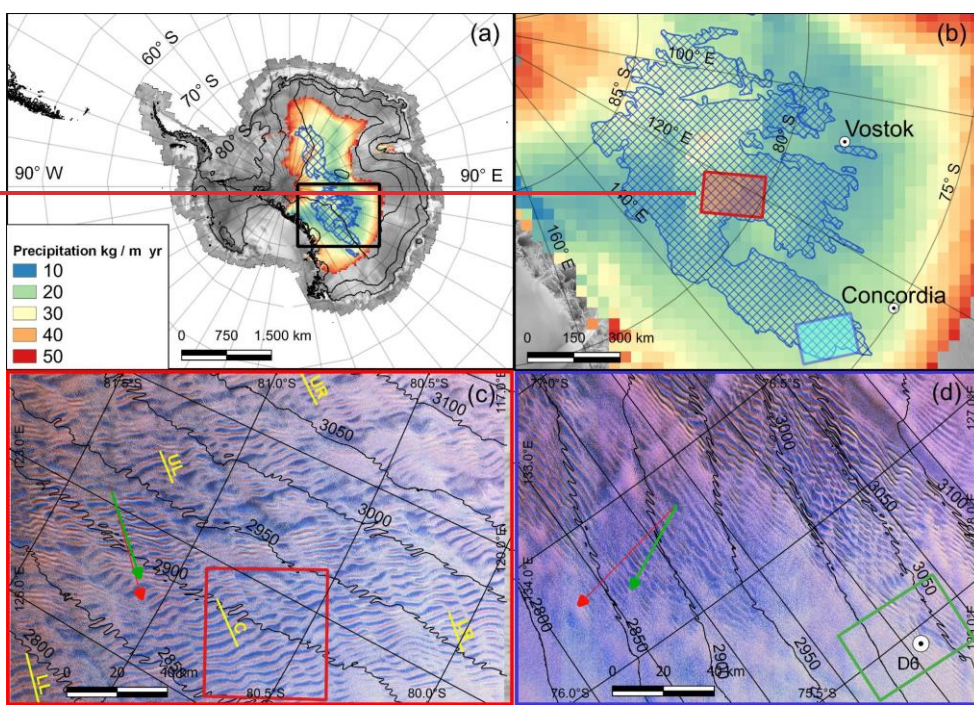
Megadune fields on the Antarctic continent extend along 10° in latitude (75°-85°S, about 1100 km) and 30° in 90 longitude (110°-140° E, about 300-600 km). The climatic conditions of the area are characterised by extremely low temperatures (mean annual temperatures from -45° to -60°C), extremely low snow precipitation (<30 mm water equivalent per year, w.e.a⁻¹; Van Wessem et al., 2014; Agosta et al., 2019) and nearly constant katabatic wind direction and wind speed (6-12 m s⁻¹; Courville et al., 2007). Analysis of data acquired by the Cloud-Aerosol Lidar and Infrared Pathfinder Satellite Observation (CALIPSO) satellite has enabled the construction of a 12-year climatology of blowing snow over Antarctica, showing that the greatest frequency of blowing snow events, approaching 75% of observations, is seen in the megadune region (Palm et al., 2019).

95 This research focuses on two megadune areas that were crossed and surveyed by two snow traverse expeditions: EAIIST (East Antarctic International Ice Sheet Traverse) in 2018-19 and It-ITASE (Italian-International TransAntarctic Scientific Expedition) in 1998-1999. EAIIST area is situated 300 km East of Vostok Station (centred at 80°47'S 122°19'E) and It-ITASE area 150 km East of Concordia Station (centred at 75°54'S 131°36'E; Fig. 1). -The survey data of the first area (EAIIST, <https://www.eaiist.com/en/>) are under processing whereas the *in situ* observations of the second traverse It-ITASE are available

ha formattato: Tipo di carattere: Corsivo

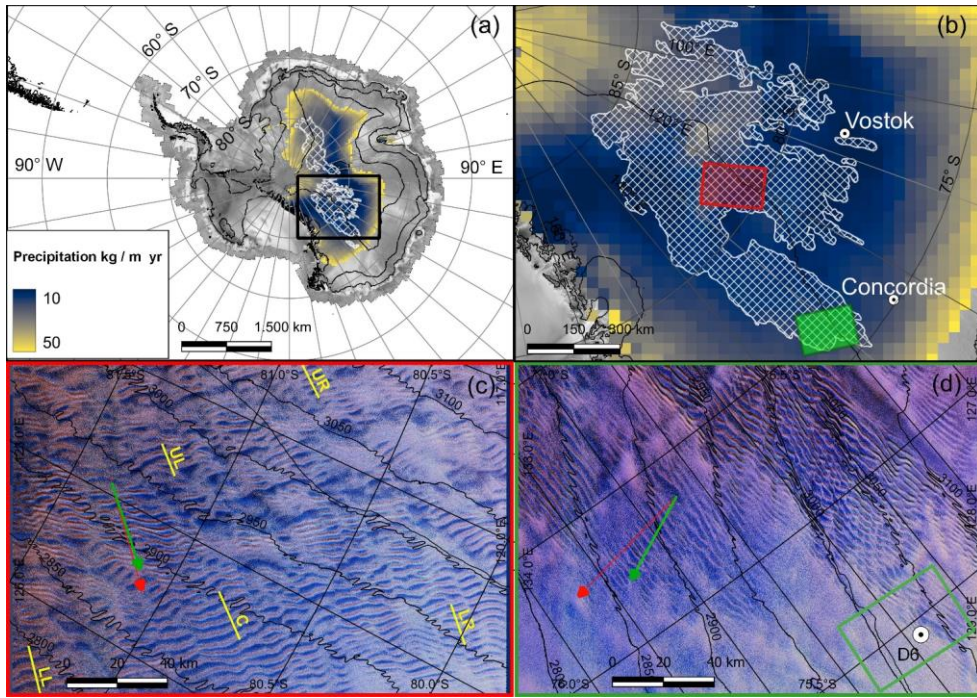
100 (Frezzotti et al., 2002a, b, 2004, 2005; Proposito et al., 2002; Vittuari et al., 2004). The EAIIST area is in the middle of the megadune area; thus, megadunes are well defined and continuous on satellite images in optical and microwave bands, whereas the It-ITASE area is at the North-East limit of the megadune field where this morphology is discontinuous and disappears, thus representing the developing threshold of the environmental conditions (morphology, climatology, glaciology) determining megadune formation.

105



ha formattato: Tipo di carattere: Calibri, 12 pt

Formattato: SpazioDopo: 8 pt, Interlinea: multipla 1.08 ri, Bordo: Superiore: (Nessun bordo), Inferiore: (Nessun bordo), A sinistra: (Nessun bordo), A destra: (Nessun bordo), Tra : (Nessun bordo)



110 Figure 1: Location map of megadune area: (a) Satellite image map of the Antarctic continent (Jezek, 1999) with elevation contour lines at 1000 m a.s.l. intervals, megadune regions are shown as cross-hatched blue/white areas (Fahnestock et al., 2000), with snow precipitation by [RAMCORACMO](#) in colour for areas with precipitation < 50 kg m² a⁻¹ (Van Wessem et al., 2014), black rectangle (b box). (b) The megadune field with two study sites, EAIIST red rectangle (c box) and It-ITASE blue/green rectangle (d box). (c) Landsat 8 OLI image in false colour (069119 scene, 17/Dec/2015) of the EAIIST area; the red polygon is the area for the analysis of variations of glazed surfaces (Fig. 4). (d) Landsat 8 OLI image in false colour (081114 on 18/Dec/2014) of the It-ITASE area and D6 core site; the green rectangle shows the location of Fig. 5d. In (c) and (d) boxes, red arrows represent ERA5 wind direction and green arrows sastrugi-based wind direction, while the yellow lines show the location of the transects studied.

115 Topographically, the two study areas are in a relative sloping zone where the altitude decreases moving from SW to NE and the elevation ranges from 2700 to 3200 m a.s.l. Thus, the topographic aspect (the direction that a topographic slope faces) is generally East (~ 80°, It-ITASE and ~ 70°, EAIIST). The regional topographic slope (10 km scale) is on average 1.5 m km⁻¹ and 1.8 m km⁻¹ for the It-ITASE and EAIIST areas, respectively. The katabatic wind direction is nearly constant with wind blowing from SW in both areas.

2 Data and Methods

2.1 Data

In order to study the megadune areas, we combined three main datasets (satellite images, meteorological data from reanalysis products, DEM) to create a method for the automatic detection of snow glazed surfaces. We further created tested two methods, one by creating 5 sample transects in the EAIIST area (Fig. 1c) and visually identified identifying thresholds of albedo, thermal brightness temperature (BT) and SPWD to discriminate between glazed surfaces and surrounding snow. The 5 transects were created in different areas of the megadune field and they show relatively different wind directions and topographic aspect and slope, with the aim of representing the widest possible range of SPWD values. For the second method, i.e. a maximum likelihood supervised classification, we created 30 polygons in the glazed snow area and 30 for firn, which were used to train the classification algorithm.

ha formattato: Colore carattere: Automatico

2.1.1 Satellite datasets

Two sources of satellite imagery were used: Landsat 8 OLI satellite images and Sentinel-2 images, both downloaded from the Earth Explorer portal (<https://earthexplorer.usgs.gov/>). Landsat 8 OLI and Sentinel-2 provide data in several spectral bands, including panchromatic, visible, very near infrared, short-wave infrared, and thermal infrared bands, with different spatial resolution from 10 to 100 m. Satellite images from Landsat 8 OLI (supplementary Table A1) were chosen at dates close to the first stripe acquisitions of the REMA DEM (2013, Table A2). The megadune area is subject to blowing snow events (more than 75% of the time; Palm et al., 2019) and cloud cover. Moreover, in the morning a strong atmospheric inversion layer develops 70 % of the time during summer on the Antarctic plateau (Pietroni et al., 2014) with the formation of fog, which is not homogeneously distributed on the area surveyed by satellite images and is difficult to detect. Therefore, we excluded from our dataset all images with cloud cover > 10% of land surface, visible blowing snow and fog events and images with solar zenith angle (SZA) $\geq 75^\circ$ (because of the effect on the albedo, as demonstrated by Picard et al., 2016), and obtained 17 images from Landsat 8 from 2013 to 2020 and 4 images from Sentinel-2 from 2018 to 2021 (Table A1), 11 for the EAIIST site and 6 for It-ITASE. To map glazed surfaces on megadunes, we used Landsat 8 OLI data as the method relies on the calculation of the albedo, which has been thoroughly validated for Landsat 8 OLI (Traversa et al., 2021a). Additionally, Landsat 8 OLI is available for a longer period of time compared to Sentinel-2, allowing us to investigate temporal evolution of the megadune area. In the megadune area, the difference between snow glazed surfaces and snow is higher considering NIR spectral albedo and brightness temperatureBT (Traversa et al., 2021b). To a “higher” amount of solar radiation absorbed by the glazed surface, corresponds also a different brightness temperatureBT on snow glazed surfaces (Fujii et al., 1987; Scambos et al., 2012 and references therein). In fact, these zones show a higher brightness temperatureBT compared to the upwind part of the dune characterised by the snow surface. In detail, we used Landsat 8 OLI Near InfraRed band (NIR band 5, with a ground resolution of 30 m) to calculate NIR albedo and thermal infrared (TIRS 1) band 10 to calculate brightness temperatureBT (with a ground resolution of 100 m, provided resampled to 30 m). To perform the megadune migration analysis (sect 2.2.2), we used the

155 panchromatic band of Landsat 8 OLI, as this band has a higher resolution (15 m) compared to the other spectral bands of ~~the~~
Landsat. For comparison, Sentinel-2 images were also used, specifically Band 8 NIR (10 m spatial resolution), which allows
better observing differences between snow and glazed surfaces compared to the other visible and infrared bands.

2.1.2 Atmospheric reanalysis dataset

We extracted wind direction from the ERA5 atmospheric reanalysis global climate dataset (Hersbach et al., 2020) and by
160 identification of sastrugi based on Landsat (Sect. 2.2.1). In particular, we used ERA5 *hourly data* (DOI:
10.24381/cds.adbb2d47) of wind speed and direction at 10 m above the surface averaged over a 20-year temporal period, from
2000 to 2019. Beside using all wind speed observations, we further divided wind speed in 5 classes, only considering wind
speed values above specific thresholds, i.e., wind speed >3 m s^{-1} , >5 m s^{-1} , >7 m s^{-1} and >11 m s^{-1} . These thresholds were
chosen based on the interactions between wind and snow: snow transportation by saltation (within 0.3 m in elevation) starts at
165 wind speeds between 2 and 5 m s^{-1} , transportation by suspension (drift snow) starts at velocities >5 m s^{-1} (within 2 m) and
blowing snow (snow transportation higher than 2 m) starts at velocities between 7 and 11 m s^{-1} (see Frezzotti et al., 2004 and
references therein). The threshold wind speed at which the sublimation of blowing snow starts to contribute substantially to
katabatic flows in a feedback mechanism appears to be 11 m s^{-1} (Kodama et al., 1985; Wendler et al., 1993).

2.1.3 Topographic dataset (DEM)

170 In order to obtain the aspect and slope of the surface for the SPWD calculation and perform topographic correction for the
calculation of albedo, we used a mosaic of REMA tiles (www.pgc.umn.edu/data/rema/; Howat et al., 2019). These are
constructed from thousands of individual stereoscopic Digital Terrain Models (DEMs) at high spatial resolution (8 m). Each
individual DEM was vertically registered to satellite altimetry measurements from Cryosat-2 and ICESat, resulting in absolute
uncertainties of less than 1 m, and relative uncertainties of ~~decimeters~~~~decimetres~~. REMA is based mainly on imagery acquired
175 during the austral summer period (December-March) and at the two sites, the temporal period is from 2008 to 2017, although
87.5% of stripes were acquired in 2013-2017 (Table A2).

2.2 Methods

The study includes four main processing steps: Landsat 8 OLI image processing for the calculation of NIR albedo; extraction
180 of thermal ~~brightness temperatures~~~~BT~~ from the Landsat thermal band 10; SPWD calculation from ERA5 and satellite sastrugi-
based wind direction, estimation of the surface velocity and migration of megadunes using feature tracking (2014-2021) and

comparison of GPR-GPS measurements from 1999 with the REMA DEM from 2014 (specific strip on the area). The first three steps were at the basis of the automatic detection of the snow glazed areas.

2.2.1 Automatic detection of glazed snow surfaces

185 ~~Taking advantage of the~~ ~~By using~~ spectral ~~datasets~~ and topographic ~~datasets employed~~~~data~~, we consider for the automatic detection of the glazed areas the following parameters: NIR albedo, thermal ~~brightness temperature~~~~BT~~ and SPWD. ~~The~~ NIR albedo (α), was here estimated using Landsat 8 OLI imagery, following the method first proposed by Klok et al. (2003) and recently tested and validated in Antarctica by Traversa et al. (2021a). We used NIR albedo as opposed to broadband albedo owing to the higher detection ability of NIR albedo, which stems from the fact that broadband albedo obtained by using Liang conversion algorithm (Liang, 2001) considers the visible area of the spectrum and the shortwave infrared. In fact, in broadband albedo it is hardly possible to recognize the differences between glazed and unglazed areas, which in the visible wavelengths look very similar (Warren, 1982).

190 Following the methodology proposed by Traversa et al. (2021a, c), the images were processed through three main steps: 1) conversion of radiance to Top of Atmosphere (TOA) reflectance by using per-pixel values of the SZA available through the Landsat solar zenith band. This conversion allows applying a more accurate per-pixel correction for the SZA, useful in our 195 study considering the average high SZA (always $\geq 59^\circ$, Table A1), and its strong effect on albedo (Pirazzini, 2004; Picard et al., 2016; Traversa et al., 2019); 2) atmospheric correction; 3) topographic correction.

To retrieve the thermal ~~brightness temperature~~~~BT~~, we employed ~~the~~ band 10 of Landsat 8. To estimate the TOA thermal ~~brightness temperature~~~~BT~~ received at the satellite, spectral radiance in the thermal band was converted using the thermal constants in the Landsat metadata (Zanter, 2019).

200 For the SPWD, the wind directions were extracted at low spatial resolution (30 km) using ERA5 and validated by identifying sastrugi and deriving wind directions from them using Landsat 8 OLI at 30 m spatial resolution (Mather, 1962; Parish and Bromwich, 1991). The identification of sastrugi was performed on the Landsat 8 OLI NIR band (band 5) by applying the Canny edge detection algorithm (*i.edge* in GRASS GIS, Canny, 1986). Prior to edge detection, each image was pre-processed by using a high pass filter with a length scale of 150 m implemented through a Fast Fourier Transform to highlight the sastrugi.

205 This process was applied on 7 Landsat scenes from the spring and summer months i.e., November, December and January of the period 2013-2020.

To further estimate the SPWD based on the wind direction from ERA5 and Landsat-derived sastrugi, we used the approach of Scambos et al. (2012), i.e., we calculated the dot product between the slope derived from the REMA DEM and the wind direction. The algorithm was applied to ERA5 and sastrugi-based wind directions resampled at 120 m spatial resolution, and 210 the REMA DEM was resampled to match ERA5 and sastrugi-based wind directions using bilinear interpolation. The resulting SPWD has units of m km^{-1} .

Due to the small difference in NIR albedo and ~~brightness temperature~~~~BT~~ of glazed surfaces (leeward) and sastrugi (windward) and the different illumination and meteorological conditions ~~inside~~~~of~~ the satellite images, the analysis of the variability of

SPWD, NIR albedo and brightness temperatureBT was conducted in detail on the 5five transects perpendicular to megadunes.

215

The comparisons were conducted using the albedo and temperature values and normalised using mean and standard deviation for each transect. Moreover, we determined the strength of the relationship between SPWD vs NIR albedo, and SPWD vs thermal brightness temperatureBT (applied on the moving averages of 11 pixels weighted based on the distance from the central point) using linear regression. The comparison analysis was conducted at seasonal scale for the 2013-2014 (4 images) and at pluriannualmulti-annual scale on 17 images distributed over 8 years.

220

~~—After having visually identified the thresholds of SPWD, NIR albedo and thermal brightness temperature on the image from 17/Dec/2015, which was one of the best available images in terms of cloud cover (~0%) and presenting no blowing snow/fog and the lowest SZA (67°) for the EAIIST site, we applied a conditional calculation to automatically map glazed snow. In order to better define the detection method and evaluate the use of each parameter, we first applied the automatic detection on the entire tile of Landsat (path 69, row 119; ~36,000 km²) and then on a narrower area (~2,400 km²), which showed higher homogeneity in NIR and TIRS 1 bands. Different thresholds of NIR albedo and thermal brightness temperature were used, which allowed the detection of the highest amount of glazed snow surface in the entire analysed area. The thresholds were defined as follows: NIR albedo < 0.82 and thermal brightness temperature > 246.5 K on the entire tile and NIR albedo < 0.805 and thermal brightness temperature > 247.6 K on the narrower area. Additionally, to determine the role of the SPWD in the automatic detection, we performed the classification by first excluding and then including this parameter (SPWD > 1 m km⁻²).~~

230

With the aim of providing an automatic methodology for distinguishing the glazed snow from the surrounding firn surface and evaluate the role of SPWD in the classification, we applied and compared two different approaches: a supervised classification (maximum likelihood) and a self-defined-threshold approach. In both cases, we considered SPWD, NIR albedo and thermal BT. The analysed images were the one from 17-Dec-2015, which was one of the best available images in terms of cloud cover (~0%), presenting no blowing snow/fog and the lowest SZA (67°) for the EAIIST site and the closest date to the REMA DEM in the area (January-October 2016), and the four scenes available for the 2013-2014 season (i.e., 25-Nov-2013, 11-Dec-2013, 27-Dec-2013 and 28-Jan-2014). For the self-defined-threshold method, we applied a conditional calculation to automatically map glazed snow. The thresholds were defined as follows: NIR albedo < 0.82, thermal BT > 246.5° K and SPWD > 1 m km⁻².

235

¹ In order to evaluate the role of each parameter, with a particular attention to the SPWD, we repeated the two approaches by using individual parameters (NIR, SPWD, BT) and combinations of them (i.e., NIR-SPWD, NIR-BT, BT-SPWD and NIR-BT-SPWD). Finally, we calculated the accuracy for each case, by creating a set of random points (100 points, following the density used in Azzoni et al., 2016) as ground truth (visually assigned on the false colour image) and comparing the results through a confusion matrix. The accuracy was calculated both for methodologies in their entirety (identifying and

245 distinguishing glazed snow and the surrounding firm surface), but also with respect to their specific ability in detecting glazed snow.

2.2.2 Megadune movement estimation

ha formattato: Francese (Francia)

250 Frezzotti et al. (2002b) and Ekyakin et al. (2015), based on the sedimentary structure of buried megadunes (using GPR and GPS), pointed out that the megadune migration and ice sheet surface flow show a similar intensity but opposite directions; difference between topographic slope and SPWD- and that megadunes migrates upwind with time, burying the glazed surface of the leeward face.

255 By Here, by using different satellite images and field data, we are able to provide and quantify megadune migration components: ice-flow (I_f) direction, which is correlated mainly to topographic slope, sedimentological migration (M_s), caused by sedimentological processes linked to deposition (on the upstream dune flank) and ablation (on the downstream dune flank) of snow, and the result of these processes, the absolute migration (M_a):

$$260 \quad \overrightarrow{M_a} = \overrightarrow{M_s} + \overrightarrow{I_f} \quad (1)$$

265 During the It-ITASE traverse at the D6 site, megadunes were surveyed by means of GPR-GPS to measure ice velocity, surface elevation and internal layering of present and buried megadunes. We compared these measurements with the REMA DEM derived by satellite images acquired in 2014 to estimate the change in surface morphology due to sedimentological migration of the megadunes. With the aim of calculating the surface velocity and direction of megadune movement, the feature tracking module *IMCORR* (Fahnestock et al., 1992; Scambos et al., 1992) was run in *System for Automated Geoscientific Analyses* (SAGA GIS). This algorithm performs image correlation based on two images providing the displacement of each pixel between the second and first image (Jawak et al., 2018). Prior to feature tracking, each image pair was pre-processed by using a low pass filter with a length scale of 150 m implemented through a Fast Fourier Transform to smooth out the sastrugi and leave megadune features for tracking. Finally, by dividing the displacement values obtained through IMCORR by the corresponding time period, we obtained the absolute migration of the megadunes in $m\ a^{-1}$. For comparison, we also employed another method to evaluate the megadune migration. By using Landsat 8 OLI imagery, similarly to what already done for the detection of sastrugi and applying an edge detection on band 5 (NIR), it is possible to identify the megadune crest and trough at the edges between leeward (glazed snow) and windward (sastrugi) zones. The obtained direction raster was manually cleaned from errors and artefacts (angles $< 200^\circ$ and $> 240^\circ$, intensity $< 5\ m\ a^{-1}$), and then vectorized after thinning, i.e., reducing the number of cells used to represent the width of the features to 1 pixel. Comparing the obtained velocity fields in different years, we could observe the absolute migration of the megadunes.

270 We considered the widest temporal interval between two pairs of cloud-free images of Landsat 8 (4 pairs) and Sentinel-2 (2 pairs), that were in a similar period of the year, to avoid relevant differences in the SZA that could confound the feature tracking algorithm (Table 1).

Zone	Satellite	t_0	t_1	t span (a)	Mean M_a (m a ⁻¹)	STD M_a (m a ⁻¹)	Features
It-ITASE	L8	02-Dec-2014	30-Nov-2019	5	14.0	3.9	30073
It-ITASE	L8	02-Dec-2014	02-Dec-2020	6	12.8	3.4	30538
It-ITASE	S2	13-Dec-2016	27-Dec-2020	4	11.4	3.8	537304
EAIIST	L8	27-Dec-2013	28-Dec-2019	6	11.9	3.6	316951
EAIIST	L8	17-Dec-2015	30-Dec-2020	5	14.2	3.4	139622
EAIIST	S2	10-Jan-2018	02-Jan-2021	3	10.5	4.1	1329648

275 **Table 1. Results of the absolute migration of megadunes calculated from IMCORR based on Landsat 8 OLI (L8) and Sentinel-2 (S2) imagery at the It-ITASE and EAIIST sites.**

280 The results from IMCORR and GPS observations were compared with the *MEASUREs ice-flow velocity* product (Rignot et al., 2017), that provides the highest-resolution (450 m) digital mosaic of ice motion in Antarctica (assembled from multiple satellite interferometric synthetic-aperture radar systems, mostly between 2007-2009 and 2013-2016), showing for each pixel the direction and the velocity of ice flow with a mean error of 3-4%.

3 Results

3.1 Megadune characterization and automatic detection

285 On average, in the 5five analysed transects NIR albedo ranges from 0.81 to 0.86 (α) in the upwind area (snow sastrugi) and from 0.73 to 0.81 (α) downwind (glazed surfaces), with differences inside the transects of about 0.07 (α) with a maximum value of 0.1 (α). The maximum contrast of NIR albedo between glazed surfaces and snow sastrugi usually occurs at springtime (October-November) and decreases during the summer season (Fig. 2). Our remote sensing observations agree with previous analysis that pointed out that in late summer, radiative cooling of the uppermost surface layer leads to formation of a surface frost, by condensation of local atmospheric vapour onto the snow surface; this gives the glazed surface a more diffuse specular reflection than in spring and changes its appearance in albedo and **brightness temperature**BT (Scambos et al., 2012 and references therein). Along the transects, the correlation of NIR albedo from the different images is high (R^2 up to 0.99) during the spring season (24 Nov 2013, 27 Dic 2013) and decreases by the end of the summer and in comparison with the following years, with an R^2 of 0.7 only after 2 years (17 Dec 2015) and up to 0.6 after 6 years (Dec 2019). A Similar decrease in correlation occurs from the comparison of the SPWD and NIR albedo from 2013 (R^2 0.66) to 2019 (R^2 0.39).

290 For the thermal **brightness temperature**BT, we observed an intra-seasonal trend on all transects: in fact, while thermal **brightness temperature**BT remains \geq 244 K during the middle of the summer (11-Dec-2013 and 27-Dec-2013), it decreases moving away from the summer solstice. Temperatures range between 238 K and 240.5 K on 25-Nov-2013, 26 days from the

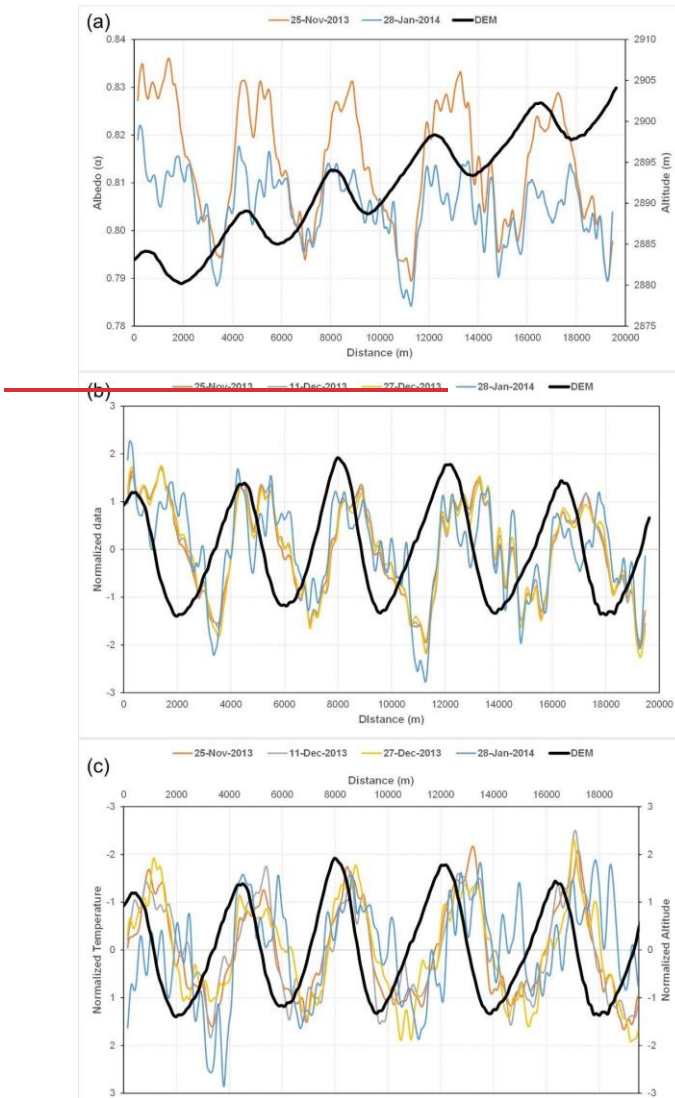
solstice. The difference increases on the date farthest from the solstice, 28-Jan-2014 (38 days from the solstice), with the lowest values ranging between 236 K and 239 K. The [brightness-temperatureBT](#) varies up to 1.5 K for each transect, but up to 3-4 K within individual images. Intra-annually, the difference between glazed surfaces and snow is higher during the spring (max 1 K in November) and tends to decrease over time, becoming lower than 0.5 K at the end of summer (January), where differences between the two surfaces are hardly detectable and the correlation between the two parameters frequently decreases drastically. These differences are directly correlated to the ones observed in NIR albedo, as a higher quantity of energy is absorbed on glazed surfaces.

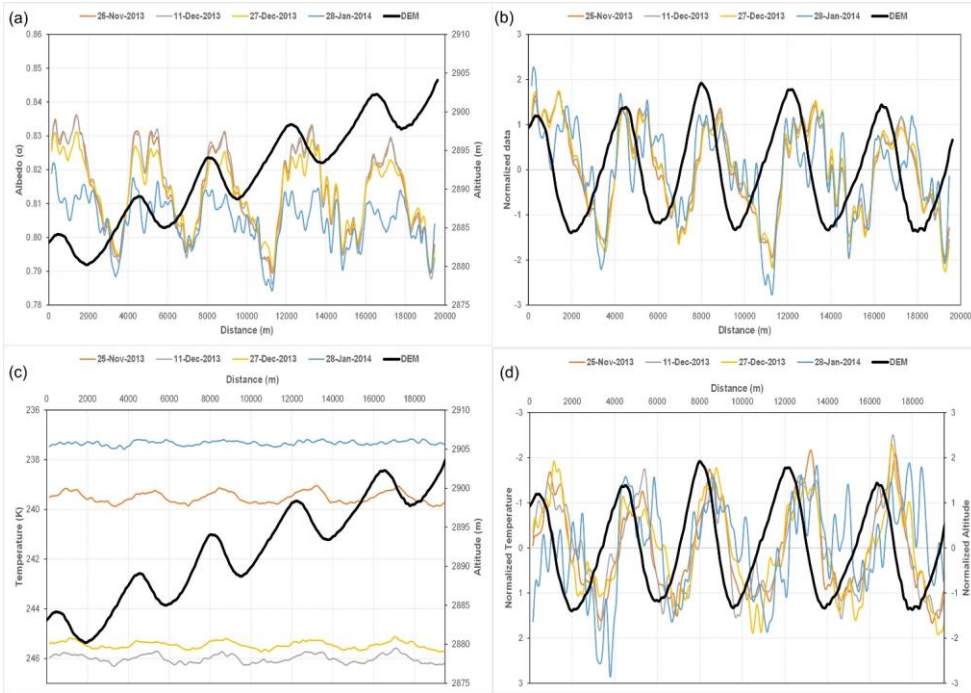
300

305

ha formattato: Tipo di carattere: Calibri, 12 pt

Formatto: Allineato al centro, SpazioPrima: 6 pt, Dopo: 6 pt, Interlinea: multipla 1.08 ri



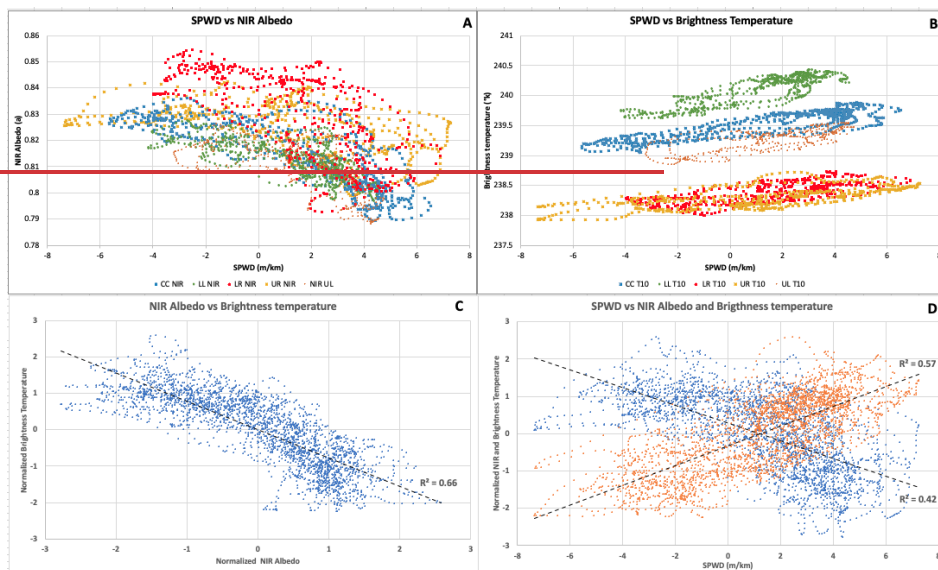


310 Figure 2: (a) moving average (based on 11 transect pixels) of NIR albedo (a) between November 2013 and February 2014 for transect
 C at the EAIIST site (see Fig. 1c for location) and elevation from REMA DEM. Corresponding normalised moving average of NIR
 315 albedo (b) and thermal **brightness temperature** **BT** TIRS1 (c) during the austral summer season 2013-2014 for transect C and
 elevation from REMA DEM (detrended topography).

High correlations are found between NIR albedo and thermal **brightness temperature** **BT** with a R^2 up to 0.67 (95% confidence
 320 interval) and between SPWD versus NIR albedo and thermal **brightness temperature** **BT** ($R^2 = 0.44$ and 0.57 at 95% confidence
 interval, respectively) calculated along all the transects (Fig. 3). The comparison between thermal **brightness temperature** **BT**
 and SPWD shows the same pattern observed for the NIR albedo, but proportionally inverse with respect to SPWD (Fig. 3),
 with higher temperatures corresponding to the glazed part of downwind areas of the dunes and conversely, lower values related
 to snow sastrugi in the upwind zones, *in accordance with previous authors (e.g., Fujii et al., 1987; Seambos et al., 2012)*.

*On Based on the basis of transects, the transect observations, the highest variabilities variability in NIR albedo and thermal
 brightness temperature at seasonal (spring-summer) to pluriannual scale is observed to be twice as large in the snow*

accumulation area on the upwind flank and the bottom of the leeward flank (Fig. 2), whereas ^{2) compared to} the glazed surface NIR albedo ^{and thermal brightness temperature remain}(0.7% compared to 0.3% NIR albedo variability), which remains more stable and more highly correlated at seasonal (spring-summer) and pluriannual scale.



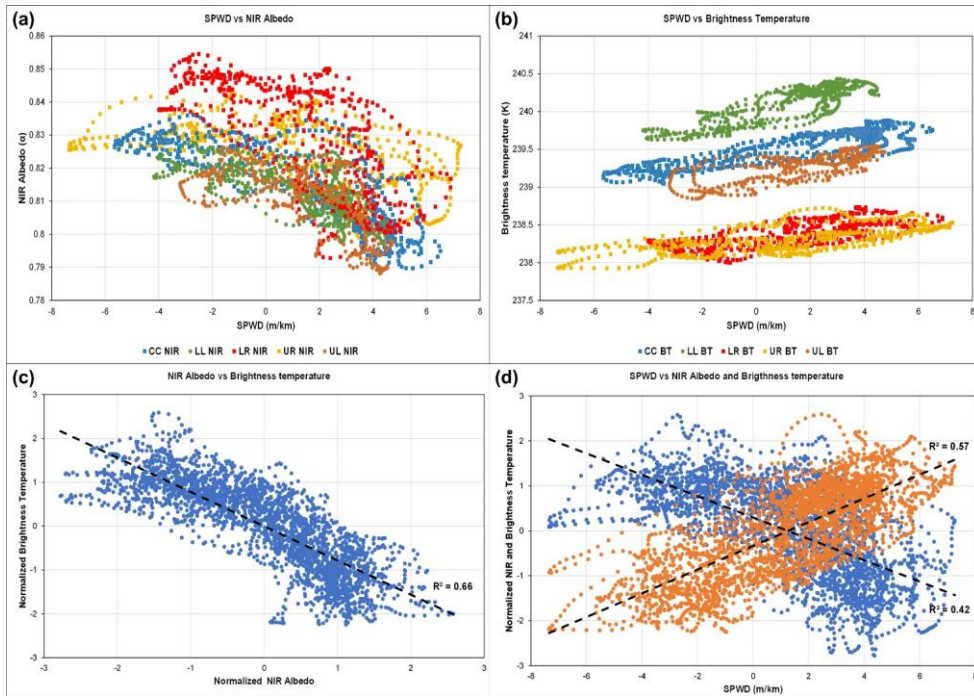


Figure 3: Diagram plots of transects at the EAIIST site from a Landsat 8 image acquired on 25-Nov-2013: (A) SPWD (slope along the prevailing wind direction) compared within each transect (C, LL, LR, UL, UR; Fig. 1 for location) with NIR spectral albedo and (B) thermal **brightness temperature**BT; (C) normalised NIR albedo of all transects compared with **brightness temperature**BT with linear regression; (D) SPWD compared with normalised NIR albedo and thermal **brightness temperature**BT for all transects with linear regression.

The analysis of sastrugi direction using [7seven](#) Landsat scenes from the spring and summer months during the period 2013-2020 show small differences in direction within each image and in repeated imagery ($< 5^\circ$), confirming the stability in direction of sastrugi landforms and thus the persistence of katabatic wind.

The comparison of the results of wind direction obtained using sastrugi direction by satellite (resampled using bilinear interpolation) and ERA5 present similar values for both areas, with lower difference in the EAIIST area (differences of 1° in average values) compared to It-ITASE (9 - 14° , see Table A3).

At the regional scale (30 km spatial resolution), the entire megadune field has an average SPWD of 1.2 m km^{-1} , when calculated using sastrugi-based wind direction, and 1.1 m km^{-1} when using ERA5, in agreement with previous studies (e.g., Frezzotti et al., 2002b). To distinguish between leeward (glazed surface) and windward flanks of the dunes for the two sites, the SPWD based on sastrugi was further resampled to 120 m using bilinear interpolation. For the SPWD on megadunes, at local scale (hundred meter), we found a mean value of $5.6 \pm 1.0 \text{ m km}^{-1}$ for the leeward side and negative SPWD values, with a mean of $-4.2 \pm 1.6 \text{ m km}^{-1}$ on the windward flanks.

Applying the automatic detection on the entire Landsat scene from 17 Dec 2015, when excluding the SPWD, approximately 34% of the entire tile was detected as glazed snow, compared to 24% using also SPWD. On the smaller area instead, a slight variation was detected with and without SPWD (22% and 23% respectively). Clipping the glazed snow surface estimated on the entire Landsat 8 tile by using the tile-based thresholds to the extent of the narrower area, an overestimation of 70% was found in comparison with the results obtained directly on the smaller area with the area-specific thresholds and when using the SPWD, rising to +88% without SPWD (Fig. 4).

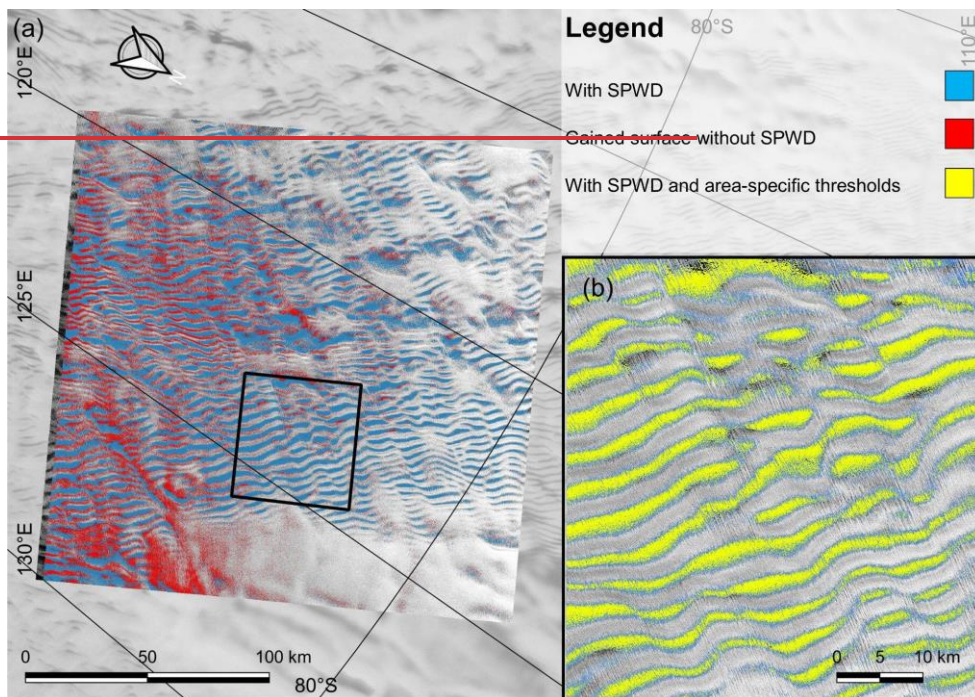


Figure 4: (a) wind-glazed surface automatic detection at the EAHIST site with the inclusion of an SPWD threshold in blue, and the overestimated detected surface when no SPWD was used. (b) the sample narrow area with thresholds defined on the entire tile of Landsat for NIR-albedo and thermal brightness temperature (blue) and with thresholds defined on the smaller area (yellow).

355

The application of the supervised classification and the self-defined-threshold methodology on the different combination of the analysed parameters, for the 2013-2014 season and on the 17/Dec/2015 scene showed contrasting results (Table 2).

Date	NIR	BT-SPWD	NIR-SPWD	NIR-BT	NIR-BT-SPWD
<u>25-Nov-2013</u>	<u>32%</u>	<u>57%</u>	<u>55%</u>	<u>9%</u>	<u>55%</u>
<u>11-Dec-2013</u>	<u>27%</u>	<u>52%</u>	<u>50%</u>	<u>32%</u>	<u>55%</u>
<u>27-Dec-2013</u>	<u>9%</u>	<u>43%</u>	<u>50%</u>	<u>9%</u>	<u>45%</u>
<u>28-Jan-2014</u>	<u>23%</u>	<u>43%</u>	<u>45%</u>	<u>23%</u>	<u>50%</u>
<u>Season average</u>	<u>$23 \pm 9\%$</u>	<u>$49 \pm 6\%$</u>	<u>$50 \pm 3\%$</u>	<u>$18 \pm 10\%$</u>	<u>$51 \pm 4\%$</u>
<u>17-Dec-2015</u>	<u>78%</u>	<u>48%</u>	<u>83%</u>	<u>70%</u>	<u>78%</u>

Table 2: accuracy assessment (%) in the detection of glazed snow using a supervised classification applied on NIR, BT and SPWD and their combination over the four scenes of 2013-2014 summer season and on 17-Dec-2015. The results of BT and SPWD (alone) are not reported, as they present the same result in all cases (i.e., 0% for BT and 30% for SPWD).

360

In fact, even if the general accuracy in distinguishing firm and glazed surfaces was on average high (mostly > 80%), with the highest values on the scene from 17-Dec-2015 (up to 94% and 98% in the combination of NIR-SPWD for supervised and self-defined thresholds respectively), lower values and higher differences were found when comparing the accuracy in detecting only glazed snow. There, the inclusion of SPWD in the classification significantly improves the ability to detect these surfaces, with a doubling of the accuracy during the season 2013-2014 (between 0% and 30% for single parameters or combination without SPWD, to around 50% of season average in the other cases, and up to 55% for NIR-BT-SPWD combination). The increase is also observed for the 17-Dec-2015 scene, from 78% of NIR alone to 83% for NIR-SPWD (which becomes 95% in the case of NIR-SPWD for self-defined-threshold methodology, the highest calculated value of accuracy in detecting glazed snow). Summarizing, the impact of the inclusion of the SPWD is evident, both applying the supervised classification and self-defined-threshold methodology, as the SPWD doubles the accuracy compared to the cases with no SPWD. We further observed issues in using BT in these approaches, because of its high heterogeneity at high scale (i.e., entire Landsat scene), as BT presents strong variations across the image; the strong improvement in using a scene (i.e., 17-Dec-2015) with no interferences (e.g., fog, clouds, “low” SZA) and close in time to the REMA DEM (stripes from January to October 2016), leading to a significant increase in accuracy of the method (from highest values of ~ 50% of scenes from season 2013-2014 to over 80%); and the higher accuracy when applying a self-defined-threshold approach.

365

370

375

3.2 Megadune migration

The absolute megadune movement calculated using feature tracking on optical satellite image pairs spans from 3 to 6 years and presents small differences in the two study areas, ranging between 10.5 m a^{-1} and 14.2 m a^{-1} overall, with no detected significant trends over time. The average values are similar when using different datasets (Landsat 8 OLI and Sentinel-2), but

380

with Sentinel-2 velocities showing slightly lower average values compared to Landsat 8. Moreover, due to the slightly higher spatial resolution (10 m versus 15 m), the number of features tracked using Sentinel-2 are an order of magnitude higher than those of Landsat 8 OLI (Table 1). The direction of the migration does not differ much across the different datasets, showing opposite values ~~with respect compared~~ to wind direction. The second method used to calculate the migration velocity is the ridge vectorization and tracking for the same image pairs. This method shows slightly higher velocities ($16.7 \pm 3 \text{ m a}^{-1}$) than

385

IMCORR tracking of megadune features ($11.9 \pm 3.6 \text{ m a}^{-1}$) at the EAIIST site for the period 2013-2019, but within the error.

At the D6 It-ITASE site, ~~5~~^{five} GPS-GPR transects were surveyed on megadunes (Frezzotti et al., 2002b); the comparison between GPS elevations (3-Jan-1999) and REMA DEM (02-Feb-2014) provides information about the relative change in elevation at high resolution (decametre level) of the megadunes during the past 15 years. On the 5 transects, we observe an almost stable elevation in correspondence with glazed surface/leeward flank, whereas the maximum difference in elevation

390

(from +1.2 to +1.9 m, with an average maximum value of +1.4 m) occurs always in the snow accumulation/upwind flank on the correspondence of the trough (Fig. [54](#)). By projecting the transects along the prevalent wind direction (239°), based on the surrounding sastrugi orientation, we were able to evaluate the megadune migration using the relative change in elevation.

Using the crest/trough position of each dune, we calculated an average displacement of $11 \pm 5.2 \text{ m a}^{-1}$ from all transects (Fig.

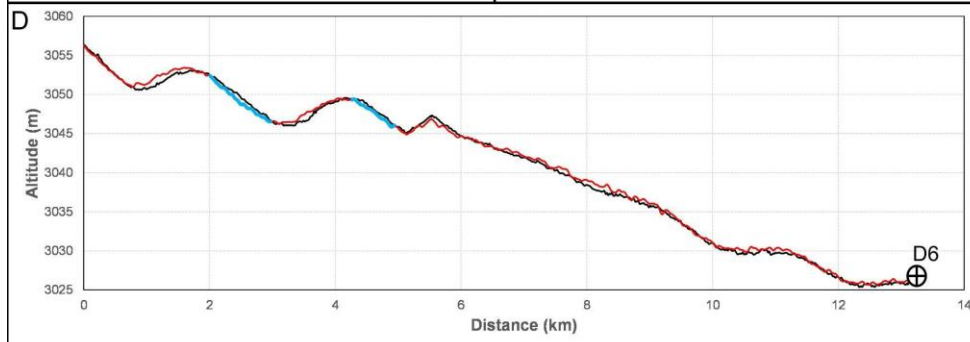
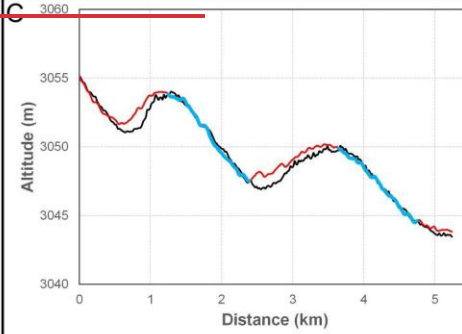
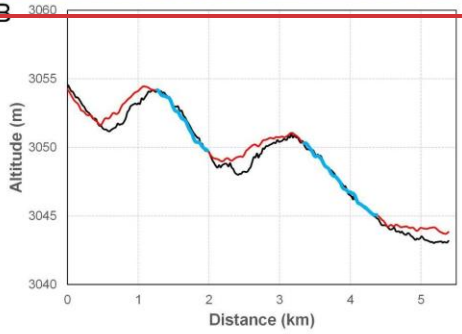
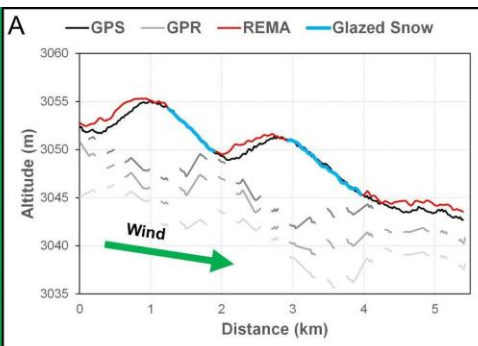
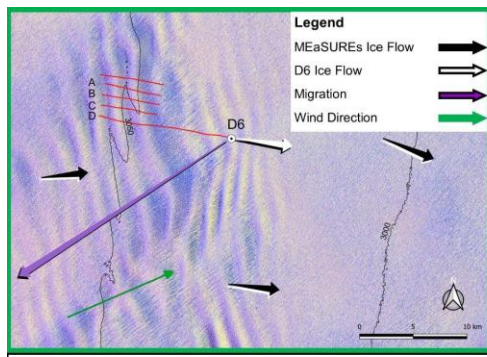
395

[54](#)). The migration of the dunes is evident in all transects with the upwind migration of the crest over the upstream flank and of the trough on the upstream flank of the previous megadune. In contrast, the glazed surfaces on the downwind flank remained

generally stable in elevation over time (Fig. [54](#)) but are clearly buried at the upstream flank foot and migrate at the crest. At the D6 site, Vittuari et al. (2004) measured an ice velocity of $1.46 \pm 0.04 \text{ m a}^{-1}$ with a direction of 97° using repeated GPS measurement between 1999 and 2001. The closer value of MEaSUREs ice flow at the D6 site is $2.2 \pm 1.1 \text{ m a}^{-1}$ with a direction of 89° , in agreement with GPS measurements. At the EAIIST site, MEaSUREs data show an ice flow of $6.1 \pm 3.4 \text{ m a}^{-1}$ with a

400

direction of $\sim 65^\circ$. Both velocity directions agree with the topographic slope at the site. Applying Eq. (1) for the calculation of megadune-migration components, we obtained a sedimentological migration of $18.4 \pm 6.7 \text{ m a}^{-1}$ (229°) at EAIIST and $15.4 \pm 4.7 \text{ m a}^{-1}$ (246°) at It-ITASE using Landsat 8 OLI data, and $16.0 \pm 7.3 \text{ m a}^{-1}$ (230°) at EAIIST and $13.6 \pm 4.9 \text{ m a}^{-1}$ (245°) at It-ITASE with Sentinel-2.



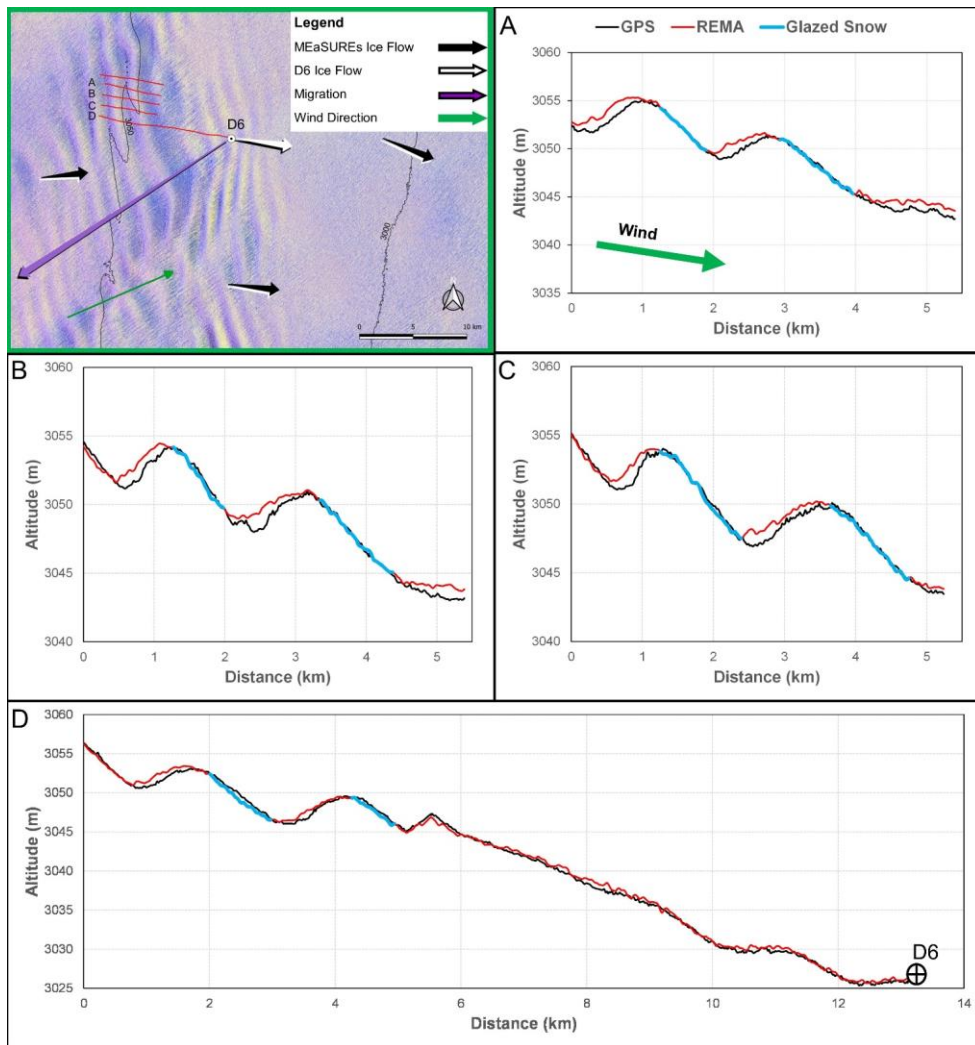


Figure 54: Location of the GPS transects (red) at the It-ITASE site with false colour Landsat 8 OLI image in background (18/Dec/2014). Universal Transverse Mercator (UTM) projection. Topographic section of four transects (A-B-C-D), with the black

lines representing elevation from in situ GPS observations (1999), red lines from REMA DEM (2014) and blue lines as glazed snow detected byon Landsat image onfrom 18-Dec-2014. In (A) we also show three GPR internal layering paleo-megadunes acquired during the It-ITASE traverse in grey shades (Frezzotti et al., 2002b).

4 Discussion

4.1 Application of the automatic detection of glazed snow on megadune fields

The satellite-derived NIR and thermal brightness temperature show large variability inside the same satellite images, in particular for thermal brightness temperature, but strong correlation among the two parameters up to a R^2 of 0.99 along each transect. The observed variabilities could be related to the different illumination condition and meteorological conditions with development of surface hoar crystal due to fog and under calm sunny weather with a downward as well as an upward vapour source to the near-surface layer. The growth of surface hoar crystals dramatically changes the snow structure, specific surface area, and density, as well as surface roughness, leading to significant changes in albedo and therefore surface temperature (Gallet et al., 2014). For these reasons, different thresholds can be required when investigating an entire tile of Landsat and a narrower area. The results from our analysis suggested the presence of a significant overestimation (at least +70%) when using thresholds defined on the entire tile and then when considering a finer scale. Nevertheless, the use of the SPWD in the automatic detection, which was possible on 17-Dec-2015 scene as the migration of megadunes in less than an year (~2016, REMA and Landsat acquisition) was lower than the spatial resolution of the used images (~10 m a⁺ vs 30 m respectively), provided better results when considering large areas (10% of overestimation when no SPWD was used), even if its inclusion appeared not so relevant in narrower areas (1% difference with and without SPWD).

In this study, we showed the possibility to calculate the SPWD based on wind direction from ERA5 and Landsat-derived sastrugi. At both investigated sites, the direction of the wind from ERA5 at velocity higher than 11 m s⁻¹ was found to be closer to the direction of sastrugi surveyed by satellite. The small difference between the two datasets could be correlated to the formation of sastrugi that is due to wind erosion processes linked to the katabatic high speed winds, as indeed closer values are detected comparing sastrugi based with high wind speed ($\geq 11 \text{ m s}^{-1}$) from ERA5. This high speed, as wind speed $\geq 11 \text{ m s}^{-1}$ was previously reported by Kodama et al. (1985) and Wendler et al. (1993) to be required for the formation of sastrugi. While the EAIIST site shows similar average directions, i.e., 221° based on sastrugi and 225° from ERA5, in the other study area (It-ITASE) a slightly higher difference was found between the two datasets for wind velocity slower than 11 m s⁻¹, reaching 13° (average 240°, max 250° minimum 215° for sastrugi based directions and average 227°, max 263° minimum 215° for ERA5). At the D6 It-ITASE site, Frezzotti et al. (2002b) pointed out that the sastrugi direction (220°–225°) measured on the field in 1998–1999 is similar (10° difference) to the sastrugi direction inferred by Landsat 7 ETM+ satellite image recorded in 2000 (230°–235°), similar to the difference observed between ERA5 and sastrugi detection by satellite in this study. The direction retrieved from Landsat is strongly dependent on high velocity prevailing winds (katabatic winds), that shape the sastrugi and direction, while ERA5 also takes into account other wind directions than the katabatic. In addition, this difference could be caused by the different spatial and temporal resolutions between the satellite and ERA5 (30 m vs 30 km,

scene-based vs average of 20 years), as well as inaccuracies in the ERA5 wind direction. The **It-ITASE site shows a** larger difference in wind direction using the various datasets (ERA5, sastrugi detected by satellite, sastrugi measured on the field); whereas the EAHOST shows a general agreement between the various datasets. This difference could at It-ITASE site could also be attributed to the higher variability of the katabatic wind direction at It-ITASE; in fact, this site is at the northern limit of megadune field (Fig. 1), and a relatively high variability of katabatic wind direction ($>10-15^\circ$) could be one of among the threshold factors that does not allow the formation of megadune on megadunes in the northern part. However, with the aim of applying this methodology at large-scale using ERA5 data, e.g., the whole continent, the differences between the two sources can be significant (e.g., at the It-ITASE site), and could produce errors in the SPWD calculation. Therefore, the use of sastrugi could be a more accurate way to interpret prevalent wind direction with high wind speed ($\geq 11 \text{ m s}^{-1}$) compared to ERA5.

The SPWD is the only parameter that could be considered as almost constant at 10s km scale, in consideration of the stability of the direction of the katabatic wind, driven mainly by surface slope and the Coriolis force. In contrast, albedo and **above all** thermal **brightness temperature continuously BT** change **both temporally**, annually and during seasons **and spatially across the satellite scene**. In fact, NIR albedo significantly varies because of surface changes up to 0.1α and between the beginning, the middle and end of the summer season in relation to the SZA by $\pm 0.01-0.02 \alpha$. Frezzotti et al., (2002b) pointed out the presence of **severe huge** sastrugi (up to 1.5 m in height) located on the windward flank and alternation of sastrugi (up to 40 cm) and glazed surfaces **are** located at the bottom of the interdune area. The observed change on NIR albedo and **brightness temperature BT** on the windward flank is correlated to the sastrugi formation and deterioration during the season, and their relative change in shadow (Warren, 1982). **While In addition**, thermal **brightness temperature BT** varies from a higher temperature near the summer solstice to lower values in late spring and summer, in the range $\pm 5-10^\circ\text{K}$. In both cases, the differences between leeward **flanks** where glazed surfaces are located and windward flanks of megadunes are not high enough to overcome the seasonal variability and thus a constant range for albedo and temperature is impossible to determine. **Spatially, the satellite derived NIR and thermal BT show large variability inside the same satellite images, in particular for thermal BT, but strong correlation among the two parameters up to a R^2 of 0.99 along each transect. The observed variabilities could be related to the different illumination condition and meteorological conditions with development of surface hoar crystal due to fog and under calm sunny weather with a downward as well as an upward vapour source to the near-surface layer. The growth of surface hoar crystals dramatically changes the snow structure, specific surface area, and density, as well as surface roughness, leading to significant changes in albedo and therefore surface temperature (Gallet et al., 2014). Therefore, different models in function of the season (beginning, middle and end) would be necessary to properly detect the two sides of each megadune using automatic methods. However, a near-constant difference between leeward and windward flanks was observed regardless of absolute values. For these reasons, different thresholds can be required when investigating an entire tile of Landsat in the case of self-defined-threshold methodology, but can also explain the inability of supervised classification based only on BT to distinguish between glazed snow and firn. With BT, in fact, the difference in values across the images is higher than the mean spectral difference between these two surfaces at these wavelengths. For the same reasons, the classification approaches**

ha formattato: Colore carattere: Automatico
ha formattato: Colore carattere: Testo 1, Non Evidenziato
ha formattato: Non Evidenziato
ha formattato: Colore carattere: Automatico

475 including BT present, in most cases, lower accuracy than the other cases, suggesting against using it to map glazed snow at large scale. On the other hand, NIR albedo does not show this sort of problem and instead demonstrates good ability in distinguishing between the two surfaces, with a good accuracy even when used alone (especially in 17-Dec-2015 case, Table 2). Additionally, it is evident how the implementation of SPWD is fundamental in aiding the detection of glazed snow, together with the NIR band, particularly by improving the detection even when the other parameters present more uncertainties (owing to e.g., SZA, fog, etc.). In fact, in all the combinations where SPWD is included, the accuracy in the distinction between glazed snow and firm shows more constant results and minimum and maximum accuracy across the analysed season is similar. Finally, our results point out the importance of using satellite images with no interferences (e.g., clouds, fog, high SZA), with the aim of automatically detecting glazed snow, as the accuracy of the method drastically increases (17-Dec-2015 compared to the other cases) and also that the self-defined-threshold approach provides better results in terms of accuracy than the supervised classification. Nevertheless, even if the self-defined-threshold model shows a higher accuracy, supervised classification allows to overcome the issue of defining accurate thresholds across a certain season, providing good accuracy results especially on good quality images, as calculated on 17-Dec-2015.

480 By using the classifications with the highest accuracy in the EAIIST area achieved based on the scene from 17-Dec-2015 (NIR-SPWD combination), where approximately 75% of the area is covered by megadunes, we could calculate that the glazed surfaces cover around 43% of this specific dune area, i.e., ~ 80% of leeward flanks.

485 In conclusion, the detection of glazed surface/ablation area by satellite images is challenging because of differences in illumination and meteorological conditions (cloud cover, blowing snow etc.) among different satellite images. Nevertheless, the high resolution digital terrain model (REMA) allows to calculate a SPWD with unprecedented detail, similar to the resolution of optical satellites (Landast 8-9, Sentinel), and significantly improves the detection of glazed/ablation surfaces at 490 ten-meter scale across the continent; therefore, it could significantly improve research on the SMB of the Antarctic Ice Sheet.

4.2 Megadune upwind migration

500 The absolute position of the megadune crest and trough are driven mainly by two processes: snow ablation/accumulation processes and ice sheet surface flow. GPS and GPR profiles along the It-ITASE traverse show the presence of paleo-megadunes buried up to the investigation depth of 20 m (Frezzotti et al., 2002b). Analysis of the D6 firn core allowed to detect the Tambora eruption signal (1816 AD) at 15.36 m depth with an average snow accumulation of 36 ± 1.8 mm w.e. a^{-1} , whereas an average value of 29 ± 7 mm w.e. a^{-1} of spatial variability in SMB at D6 site was evaluated by GPR calibrated using accumulation at three firn cores (Frezzotti et al., 2005). The elevation ~~change~~ changes during 15 years observed using GPS and REMA ~~shows~~ show a relative increase of accumulation on the windward flank with the maximum value at the trough compared to the glazed surface area from 29 to 46 mm w.e. a^{-1} with an average value of 34 mm w.e. a^{-1} , using a density of 360 kg m^{-3} in the first two metres. This value is very close to the estimated change of accumulation in the megadune area from 7 to 35 mm w.e. a^{-1} provided by Frezzotti et al., (2002b) using the variability of GPR internal layering at the megadune site (Fig. 5). The

minimum value represents a decrease in accumulation up to 75% or more on glazed surfaces. The relative stability of glazed surfaces with respect to elevation change and NIR albedo confirms the extremely stable SMB low value of the glazed surfaces with respect to accumulation ~~area~~areas, due to the long-term hiatus in SMB forced by wind scouring processes.

Using the isochrone distance of 1.5-1.8 km between the 180 years old paleo-crest detected by GPR and the recent crest from GPS observations (1998-99 AD), we can evaluate the windward migration of the paleo megadune crest at about $8-10 \text{ m a}^{-1}$. This vector from field observations summed with an ice flow from GPS of $1.46 \pm 0.04 \text{ m a}^{-1}$ with a direction of 97° produced an absolute migration of 10.3 m a^{-1} with a direction of 214° . This value is in very good agreement with absolute migration calculated using the elevation comparison between GPS and REMA ($11 \pm 5.2 \text{ m a}^{-1}$) and with satellite tracking (from 11.4 to 14.0 m a^{-1}), in particular with Sentinel-2 images (11.4 m a^{-1} , Table 1). At the D6 site, the movement components show different intensity with an order of magnitude of difference: $1-2 \text{ m a}^{-1}$ for ice flow, versus $13.6-15.4 \text{ m a}^{-1}$ for sedimentological migration. The components present nearly opposite directions: 97° for ice flow and 245° for sedimentological migration. The results allowed us to calculate all the components of migration and to conclude that for a megadune with a wavelength of 3 km we could calculate an absolute migration of approximately 10 m a^{-1} . This burying process of snow on glazed surfaces takes about 300 years, with overlap of crest to through and glazed to sastrugi surface as observed by GPR internal layering (Fig. 5).

The megadune migration on the upwind part observed by elevation change and tracking is also confirmed by the comparison of NIR and ~~brightness~~ temperature BT along the studied transects. These parameters remain relatively stable during the observed time on the glazed surface on the leeward flank, whereas the positive SMB upwind flank and bottom through area ~~changes~~change significantly at pluriannual scale, but also at seasonal scale. Hence, we observe a general overestimation of sedimentological and absolute migration using remote sensing with a mean difference of $+1.9 \text{ m a}^{-1}$ for Sentinel-2 (uncertainties of 19% for sedimentological migration and 10% for absolute migration). Using Landsat 8 OLI images, larger differences were found, with an average overestimation of 3.8 m a^{-1} . This difference could be caused by spatial variability of processes: with remote sensing we analysed a much wider area, as opposed to in situ observations which were acquired in transects on a limited section of the megadune field. Finally, the spatial resolution and geolocation (Mouginot et al., 2017) could affect the satellite data, as demonstrated by the worse results obtained using Landsat images at 15 m spatial resolution against 10 m of Sentinel-2.

The ice velocity of MEaSUREs is based on SAR images and is in ~~perfect~~very good agreement with GPS measurement, and the tracking methods of IMCORR using optical images and crest displacement is in agreement with the migration of morphologies observed from the comparison between change in elevation by GPS and REMA. ~~On the basis of~~Based on our analysis, the sedimentological processes are analogous at It-ITASE and EAIIST sites. At the second site, a faster ice-flow motion was observed by ~~MEaSURE~~MEaSURE, and the velocity of absolute migration is reduced by almost 35%, compared to the initial sedimentological-migration velocity.

The ice velocity based on SAR images presents a phase centre that penetrates up to 10 m on dry and cold firm (Rignot et al., 2001) and provides information on ice flow and not surface features. In contrast, using feature tracking on optical images

(Landsat and Sentinel-2), it is possible to estimate the absolute migration (migration + ice flow) of surface features that could be significantly different from ice flow as for the megadunes.

5 Conclusions

545 This study ~~provides new information about~~^{significantly improved} the ~~peculiar~~^{previous} knowledge on the temporal/spatial variability of Antarctic megadunes and glazed surfaces, measurements of their sedimentation/migration and their interaction between ~~with~~^{with} atmosphere and cryosphere that drives the megadune formation and evolution ice sheet surface. The snow accumulation distribution/variability processes that allow megadune formation have important consequences concerning the choice of sites for ice coring and SMB evaluation, since orographic variations of few metres per kilometre have a significant impact on the snow accumulation process. Furthermore, these new results represent a new ground truth and foundation of knowledge for ice sheet mass balance research, in particular for satellite altimeter and ice velocity derived by remote sensing measurements (e.g., radar vs optical/lidar).

550 ~~The present study significantly improved the previous knowledge on Antarctic megadune temporal/spatial variability and quantified the sedimentation/migration processes and their interaction with atmosphere and ice sheet surface. The results confirm~~^{The new results confirm and quantify the} previous hypotheses and provide new relevant information on different aspects of these peculiar landforms showing that the megadune is a dynamic feature at different spatial and temporal scales.

555 ~~In detail~~^{The glazed surface/megadune survey has revealed previously unknown large spatial variability in ice sheet SMB, superimposed on the large/scale gradients in SMB from the coast to the interior. On smaller scales (<1 km), SMB varies considerably as well, driven by surface topography undulations (SPWD) and consequent wind-driven snow ablation and redistribution, which challenges the spatial representativeness of stake and firn/ice core records. Moreover, this small-scale variability is not represented by Regional Climate Model systems used for SMB evaluation (eg. Agosta et al., 2019; Lenaerts et al., 2019), which currently operate at horizontal resolutions of typically 25 km for East Antarctica. Previous studies have pointed out that glazed areas are extensive enough to have a significant impact on current estimates of SMB, and therefore overall mass balance using the mass budget method (Frezzotti et al., 2004; Das et al., 2013; Scambos et al., 2012). The scale of the overestimation is of the same order of magnitude as the total error reported for East Antarctica and a large fraction of the currently reported error bars for Antarctic-wide mass balance (Rignot et al., 2019).}

560 Considering the characteristics of megadunes, the leeward glazed flanks show a lower NIR albedo (up to 0.1) and higher ~~brightness temperatures~~^{BT} (up to 1.5 K) compared to windward snow-covered sides within each of the ~~five~~⁵ transects analysed. NIR albedo and thermal ~~brightness temperature~~^{BT}, combined with the SPWD, allowed us to produce a method for automatically detecting glazed surfaces. High correlations were found between SPWD and NIR albedo and thermal ~~brightness temperature~~^{BT} with a R^2 up to 0.44 and 0.57 respectively calculated along the whole transect examined in 2013-14, with differences between spring and end of summer. The correlations between SPWD and NIR albedo on the transects decrease to 0.39 in comparison with the image from Dec 2019. Moreover, the high correlation of NIR albedo between images decreases over time by up to 60% between Nov 2013 and Dec 2019. Our results ~~show that on wide areas, a large overestimation is support~~

575 the detectionimportance of snow glazed surfaces (up to 88%) can result when using only NIR albedo and thermal brightness temperature in the classification, while including the SPWD substantially improves the classification results. However, when applied in narrower areas, where a higher homogeneity of NIR and TIRS1 bands is present, the inclusion of the SPWD is not so relevant, considering also the low availability of high resolution wind and topographic slope data at different temporal periods, which need to be (especially when) sufficiently synchronous with spectral imagery, in consideration of the migration of megadunes) for megadune snow characterization. Together with NIR albedo, the SPWD was found to be more important than BT in the classification, and to provide a higher accuracy than spectral data only, by allowing accuracy >80% in detecting glazed snow. Further research might consider other parameters to automatically detect snow glazed surfaces, including snow grain size or the normalised difference snow index.

580 Finally, we provided for the first time an estimation of megadune migration from field and remote observations at the It-ITASE site. The results obtained using field measurements and remote observations allow to calculate all the components of megadune migration, absolute ($11\text{--}14 \text{ m a}^{-1}$), sedimentological migration ($13\text{--}15 \text{ m a}^{-1}$) and the ice flow ($1\text{--}2 \text{ m a}^{-1}$) and to conclude that for a megadunes with a wavelength of 3 km and migration of approximately 10 m a^{-1} , the burying process of snow on glazed surfaces takes about 300 years, with overlap of crest to through and glazed to sastrugi surface.

585 The reconstruction of paleoclimate based on firn/ice cores drilled in megadune areas or downstream area is very complex. In megadune areas, the distortion of recordings is characterised by a snow accumulation/hiatus periodicity of about hundreds of years. The length of periodic variations due to mesoscale relief and/or megadunes depends on ice velocity, megadune migration and snow accumulation, and can therefore vary in space and time within the $500,000 \text{ km}^2$ of megadune field. and downstream area. In the end, our work points out the importance of “antidunal” sedimentological processes in megadune fields with an almost opposite direction between the migration of surface features and ice flow derived respectively from feature tracking of optical images and SAR. These results present significant implication for surface measurements using Radar/Lidar altimetric 590 satellite and measurements of ice flow using optical and SAR image in the megadune area. Moreover, our results point out the different elevation behaviour at pluriannual scale of the stable elevation and NIR albedo of glazed surface, while the snow-covered surface changes elevation and NIR albedo, with a higher accumulation/elevation in correspondence with the previous trough, decreasing from the trough towards the windward crest. Wind-driven process greatly affects the SMB of the megadune area, which implies that imply all or most of the regional accumulation (as determined by RACMO and other models) is gathered in the accretionary faces whereas in the downwind area the SMB is near zero with a long hiatus in snow accumulation.

Data availability

600 Data used to the aims of the present study are available from different repositories: Landsat 8 and Sentinel 2 imagery are available from <https://earthexplorer.usgs.gov/>; ERA5 data are available from <https://www.ecmwf.int/en/forecasts/datasets/reanalysis-datasets/era5> and REMA DEM from

<https://www.pgc.umn.edu/data/rema/>. Field data were obtained from ~~previous~~^{previously} published papers, i.e., Frezzotti et al. (2002a, b) and Vittorari et al. (2004).

Author contributions

GT, MF conceived the idea of this work. GT and DF developed the procedure and processed the satellite image and data. All 610 authors contributed to the writing of the final manuscript.

Competing interests

The authors declare that they have no conflict of interest.

Acknowledgments

The authors are thankful to [PNRA- National Antarctic Research Program and](#) MNA-National Antarctic Museum-of Italy 615 [respectively fellowship and](#) PhD Scholarship of G. Traversa), the Department for Regional Affairs and Autonomies (DARA) of the Italian Presidency of the Council of Ministers and Levissima Sanpellegrino S.p.A. (post-doc fellowship of D. Fugazza). This study was supported by the EAIIST project (ANR-16-CE01- 0011), the Institut Polaire Français Paul-Emile Victor (IPEV), the National Antarctic Research Program (PNRA), the French Research National Agency (Project). The authors would like to warmly thank all the participants of the It-ITASE and EAIIST traverses for their tremendous field contributions allowing 620 the collection of the crucial in situ measurements used in this study.

References

Agosta, C., Amory, C., Kittel, C., Orsi, A., Favier, V., Gallée, H., van den Broeke, M. R., Lenaerts, J. T. M., van Wessem, J. M., van de Berg, W. J., and Fettweis, X.: Estimation of the Antarctic surface mass balance using the regional climate model MAR (1979–2015) and identification of dominant processes, *The Cryosphere*, 13, 281–296, <https://doi.org/10.5194/tc-13-281-2019>, 2019.

Albert, M., Shuman, C., Courville, Z., Bauer, R., Fahnestock, M., and Scambos, T.: Extreme firn metamorphism: impact of decades of vapor transport on near-surface firn at a low-accumulation glazed site on the East Antarctic plateau, *Ann. Glaciol.*, 39, 73–78, <https://doi.org/10.3189/172756404781814041>, 2004.

Arcone, S. A., Jacobel, R., and Hamilton, G.: Unconformable stratigraphy in East Antarctica: Part I. Large firn cosets, recrystallized growth, and model evidence for intensified accumulation, *J. Glaciol.*, 58, 240–252, <https://doi.org/10.3189/2012Jo11J044>, 2012a.

Arcone, S. A., Jacobel, R., and Hamilton, G.: Unconformable stratigraphy in East Antarctica: Part II. Englacial cosets and recrystallized layers, *J. Glaciol.*, 58, 253–264, <https://doi.org/10.3189/2012JoG11J045>, 2012b.

Azzoni, R. S., Senese, A., Zerboni, A., Maugeri, M., Smiraglia, C., and Diolaiuti, G. A.: Estimating ice albedo from fine debris 635 cover quantified by a semi-automatic method: the case study of Forni Glacier, Italian Alps, *The Cryosphere*, 10, 665–679, <https://doi.org/10.5194/tc-10-665-2016>, 2016.

Bishop, M. P., Björnsson, H., Haeberli, W., Oerlemans, J., Shrader, J. F., and Tranter, M.: Encyclopedia of snow, ice and glaciers, Springer Science & Business Media, 2011.

Canny, J.: A computational approach to edge detection, *IEEE Trans. Pattern Anal. Mach. Intell.*, 679–698, 1986.

640 Courville, Z. R., Albert, M. R., Fahnestock, M. A., Cathles, L. M., and Shuman, C. A.: Impacts of an accumulation hiatus on the physical properties of firn at a low-accumulation polar site, *J. Geophys. Res.*, 112, F02030, <https://doi.org/10.1029/2005JF000429>, 2007.

645 Dadic, R., Mott, R., Horgan, H. J., and Lehning, M.: Observations, theory, and modeling of the differential accumulation of Antarctic megadunes: ACCUMULATION OF ANTARCTIC MEGADUNES, *J. Geophys. Res. Earth Surf.*, 118, 2343–2353, <https://doi.org/10.1002/2013JF002844>, 2013.

Das, I., Bell, R. E., Scambos, T. A., Wolovick, M., Creyts, T. T., Studinger, M., Frearson, N., Nicolas, J. P., Lenaerts, J. T. M., and van den Broeke, M. R.: Influence of persistent wind scour on the surface mass balance of Antarctica, *Nat. Geosci.*, 6, 367–371, <https://doi.org/10.1038/ngeo1766>, 2013.

650 Ekeykin, A. A., Lipenkov, V. Ya., and Shibaev, Yu. A.: Spatial Distribution of the Snow Accumulation Rate Along the Ice Flow Lines Between Ridge B and Lake Vostok, *Ice Snow*, 52, 122, <https://doi.org/10.15356/2076-6734-2012-4-122-128>, 2015.

Fahnestock, M. A., Scambos, T. A., and Bindschadler, R. A.: Semi-automated ice velocity determination from satellite imagery, *Eos*, 73, 493, 1992.

655 Fahnestock, M. A., Scambos, T. A., Shuman, C. A., Arthern, R. J., Winebrenner, D. P., and Kwok, R.: Snow megadune fields on the East Antarctic Plateau: Extreme atmosphere-ice interaction, *Geophys. Res. Lett.*, 27, 3719–3722, <https://doi.org/10.1029/1999GL011248>, 2000.

Foga, S., Scaramuzza, P. L., Guo, S., Zhu, Z., Dilley Jr, R. D., Beckmann, T., Schmidt, G. L., Dwyer, J. L., Hughes, M. J., and Laue, B.: Cloud detection algorithm comparison and validation for operational Landsat data products, *Remote Sens. Environ.*, 194, 379–390, <https://doi.org/10.1016/j.rse.2017.03.026>, 2017.

660 Frezzotti, M., Gandolfi, S., Marca, F. L., and Urbini, S.: Snow dunes and glazed surfaces in Antarctica: new field and remote-sensing data, *Ann. Glaciol.*, 34, 81–88, <https://doi.org/10.3189/172756402781817851>, 2002a.

Frezzotti, M., Gandolfi, S., and Urbini, S.: Snow megadunes in Antarctica: Sedimentary structure and genesis, *J. Geophys. Res. Atmospheres*, 107, A1-1-ACL 1-12, <https://doi.org/10.1029/2001JD000673>, 2002b.

665 Frezzotti, M., Pourchet, M., Flora, O., Gandolfi, S., Gay, M., Urbini, S., Vincent, C., Becagli, S., Gragnani, R., and Proposito, M.: New estimations of precipitation and surface sublimation in East Antarctica from snow accumulation measurements, *Clim. Dyn.*, 23, 803–813, <https://doi.org/10.1007/s00382-004-0462-5>, 2004.

Frezzotti, M., Pourchet, M., Flora, O., Gandolfi, S., Gay, M., Urbini, S., Vincent, C., Becagli, S., Gragnani, R., and Proposito, M.: Spatial and temporal variability of snow accumulation in East Antarctica from traverse data, *J. Glaciol.*, 51, 113–124, <https://doi.org/10.3189/172756505781829502>, 2005.

670 Fugazza, D., Senese, A., Azzoni, R. S., Maugeri, M., and Diolaiuti, G. A.: Spatial distribution of surface albedo at the Forni Glacier (Stelvio National Park, Central Italian Alps), *Cold Reg. Sci. Technol.*, 125, 128–137, <https://doi.org/10.1016/j.coldregions.2016.02.006>, 2016.

675 Fujii, Y., Yamanouchi, T., Suzuki, K., and Tanaka, S.: Comparison of the Surface Conditions of the Inland Ice Sheet, Dronning Maud Land, Antarctica. Derived from Noaa AVHRR Data with Ground Observation, *Ann. Glaciol.*, 9, 72–75, <https://doi.org/10.3189/S0260305500000410>, 1987.

Gallet, J. C., Domine, F., Savarino, J., Dumont, M., & Brun, E.: The growth of sublimation crystals and surface hoar on the Antarctic plateau, *The Cryosphere*, 8(4), 1205–1215, 2014.

680 Hersbach, H., Bell, B., Berrisford, P., Hirahara, S., Horányi, A., Muñoz-Sabater, J., Nicolas, J., Peubey, C., Radu, R., Schepers, D., Simmons, A., Soci, C., Abdalla, S., Abellán, X., Balsamo, G., Bechtold, P., Biavati, G., Bidlot, J., Bonavita, M., Chiara, G., Dahlgren, P., Dee, D., Diamantakis, M., Dragani, R., Flemming, J., Forbes, R., Fuentes, M., Geer, A., Haimberger, L., Healy, S., Hogan, R. J., Hólm, E., Janisková, M., Keeley, S., Laloyaux, P., Lopez, P., Lupu, C., Radnoti, G., Rosnay, P., Rozum, I., Vamborg, F., Villaume, S., and Thépaut, J.: The ERA5 Global Reanalysis, *Q. J. R. Meteorol. Soc.*, qj.3803, <https://doi.org/10.1002/qj.3803>, 2020.

685 Howat, I. M., Porter, C., Smith, B. E., Noh, M.-J., and Morin, P.: The Reference Elevation Model of Antarctica, *The Cryosphere*, 13, 665–674, <https://doi.org/10.5194/tc-13-665-2019>, 2019.

Jawak, S. D., Kumar, S., Luis, A. J., Bartanwala, M., Tummala, S., and Pandey, A. C.: Evaluation of geospatial tools for generating accurate glacier velocity maps from optical remote sensing data, in: Multidisciplinary Digital Publishing Institute Proceedings, 341, <https://doi.org/10.3390/ecrs-2-05154>, 2018.

690 Jezek, K. C.: Glaciological properties of the Antarctic ice sheet from RADARSAT-1 synthetic aperture radar imagery, *Ann. Glaciol.*, 29, 286–290, <https://doi.org/10.3189/172756499781820969>, 1999.

Klok, E. L., Greuell, W., and Oerlemans, J.: Temporal and spatial variation of the surface albedo of Morteratschglletscher, Switzerland, as derived from 12 Landsat images, *J. Glaciol.*, 49, 491–502, <https://doi.org/10.3189/172756503781830395>, 2003.

695 Kodama, Y., Wendler, G., and Gosink, J.: The effect of blowing snow on katabatic winds in Antarctica, *Ann. Glaciol.*, 6, 59–62, <https://doi.org/10.3189/1985AoG6-1-59-62>, 1985.

Lenaerts, J. T., Medley, B., van den Broeke, M. R., and Wouters, B.: Observing and modeling ice sheet surface mass balance, *Rev. Geophys.*, 57, 376–420, 2019.

Liang, S.: Narrowband to broadband conversions of land surface albedo I: Algorithms, *Remote Sens. Environ.*, 76, 213–238, [https://doi.org/10.1016/S0034-4257\(00\)00205-4](https://doi.org/10.1016/S0034-4257(00)00205-4), 2001.

700 Mather, K. B.: Further observations on sastrugi, snow dunes and the pattern of surface winds in Antarctica, *Polar Rec.*, 11, 158–171, <https://doi.org/10.1017/S0032247400052888>, 1962.

Mayewski, P. and Goodwin, I.: Antarctic's role pursued in global climate change, *Eos Trans. Am. Geophys. Union*, 80, 398–400, <https://doi.org/10.1029/EO080i035p00398>, 1999.

705 Meredith, M., Sommernorn, M., Cassotta, S., Derksen, C., Ekaykin, A., Hollowed, A., Kofinas, G., Mackintosh, A., Melbourne-Thomas, J., and Muelbert, M. M. C.: Polar Regions. Chapter 3, *IPCC Special Report on the Ocean and Cryosphere in a Changing Climate*, 2019.

Mouginot, J., Rignot, E., Scheuchl, B., and Millan, R.: Comprehensive annual ice sheet velocity mapping using Landsat-8, Sentinel-1, and RADARSAT-2 data, *Remote Sens.*, 9, 364, <https://doi.org/10.3390/rs9040364>, 2017.

710 Núñez-González, F. and Martín-Vide, J. P.: Analysis of antidune migration direction, *J. Geophys. Res. Earth Surf.*, 116, <https://doi.org/10.1029/2010JF001761>, 2011.

Palm, S. P., Yang, Y., Spinhirne, J. D., and Marshak, A.: Satellite remote sensing of blowing snow properties over Antarctica, *J. Geophys. Res.*, 116, D16123, <https://doi.org/10.1029/2011JD015828>, 2011.

Palm, S. P., Kayetha, V., Yang, Y., and Pauly, R.: Blowing snow sublimation and transport over Antarctica from 11 years of CALIPSO observations, *The Cryosphere*, 11, 2555–2569, <https://doi.org/10.5194/tc-11-2555-2017>, 2017.

715 Parish, T. R. and Bromwich, D. H.: Continental-scale simulation of the Antarctic katabatic wind regime, *J. Clim.*, 4, 135–146, [https://doi.org/10.1175/1520-0442\(1991\)004<0135:CSSOTA>2.0.CO;2](https://doi.org/10.1175/1520-0442(1991)004<0135:CSSOTA>2.0.CO;2), 1991.

Picard, G., Libois, Q., Arnaud, L., Verin, G., and Dumont, M.: Development and calibration of an automatic spectral albedometer to estimate near-surface snow SSA time series, *The Cryosphere*, 10, 1297–1316, <https://doi.org/10.5194/tc-10-1297-2016>, 2016.

720 Pietroni, I., Argentini, S., & Petenko, I.: One year of surface-based temperature inversions at Dome C, Antarctica. *Boundary-Layer Meteorology*, 150(1), 131–151, 2014.

Pirazzini, R.: Surface albedo measurements over Antarctic sites in summer, *J. Geophys. Res.*, 109, D20118, <https://doi.org/10.1029/2004JD004617>, 2004.

725 Proposito, M., Becagli, S., Castellano, E., Flora, O., Genoni, L., Gragnani, R., Stenni, B., Traversi, R., Udisti, R., and Frezzotti, M.: Chemical and isotopic snow variability along the 1998 ITASE traverse from Terra Nova Bay to Dome C, East Antarctica, *Ann. Glaciol.*, 35, 187–194, <https://doi.org/10.3189/172756402781817167>, 2002.

Prothero, D. R. and Schwab, F.: *Sedimentary geology*, Macmillan, 2004.

Rignot, E., Echelmeyer, K., and Krabill, W.: Penetration depth of interferometric synthetic-aperture radar signals in snow and ice, *Geophys. Res. Lett.*, 28, 3501–3504, <https://doi.org/10.1029/2000GL012484>, 2001.

730 Rignot, E., Mouginot, J., and Scheuchl, B.: MEaSUREs InSAR-based Antarctica ice velocity map, version 2, Boulder CO NASA DAAC Natl. Snow Ice Data Cent., 2017.

[Rignot, E., Mouginot, J., Scheuchl, B., van den Broeke, M., van Wessem, M. J., and Morlighem, M.: Four decades of Antarctic Ice Sheet mass balance from 1979–2017, Proc. Natl. Acad. Sci.](https://doi.org/10.1073/pnas.1812883116), 116, 1095–1103, <https://doi.org/10.1073/pnas.1812883116>, 2019.

735 Scambos, T. A., Dutkiewicz, M. J., Wilson, J. C., and Bindschadler, R. A.: Application of image cross-correlation to the measurement of glacier velocity using satellite image data, *Remote Sens. Environ.*, 42, 177–186, 1992.

Scambos, T. A., Frezzotti, M., Haran, T., Bohlander, J., Lenaerts, J. T. M., Van Den Broeke, M. R., Jezek, K., Long, D., Urbini, S., Farness, K., Neumann, T., Albert, M., and Winther, J.-G.: Extent of low-accumulation “wind glaze” areas on the East Antarctic plateau: implications for continental ice mass balance, *J. Glaciol.*, 58, 633–647, <https://doi.org/10.3189/2012JoG11J232>, 2012.

740 Schaefer-Strub, G., Schaefer, M. E., Painter, T. H., Dangel, S., and Martonchik, J. V.: Reflectance quantities in optical remote sensing—Definitions and case studies, *Remote Sens. Environ.*, 103, 27–42, <https://doi.org/10.1016/j.rse.2006.03.002>, 2006.

Swithinbank, C.: Antarctica, US Government Printing Office, 1988.

745 Traversa, G., Fugazza, D., Senese, A., and Diolaiuti, G. A.: Preliminary results on Antarctic albedo from remote sensing observations, *Geogr Fis Din Quat*, 42, 245–254, <http://dx.doi.org/10.4461/GFDQ.2019.42.14>, 2019.

Traversa, G., Fugazza, D., Senese, A., and Frezzotti, M.: Landsat 8 OLI Broadband Albedo Validation in Antarctica and Greenland, *Remote Sens.*, 13, 799, <https://doi.org/10.3390/rs13040799>, 2021a.

750 Traversa, G., Fugazza, D., and Frezzotti, M.: Analysis of Megadune Fields in Antarctica, in: 2021 IEEE International Geoscience and Remote Sensing Symposium IGARSS, 5513–5516, <https://doi.org/10.1109/IGARSS47720.2021.9554827>, 2021b.

Traversa, G. and Fugazza, D.: Evaluation of Anisotropic Correction Factors for the Calculation of Landsat 8 OLI Albedo on the Ice Sheets, *Geogr Fis Din Quar*, 44, 91–95, <http://dx.doi.org/10.4461/GFDQ.2021.44.8>, 2021c.

755 Van Wessem, J. M., Reijmer, C. H., Morlighem, M., Mouginot, J., Rignot, E., Medley, B., Joughin, I., Wouters, B., Depoorter, M. A., Bamber, J. L., Lenaerts, J. T. M., Van De Berg, W. J., Van Den Broeke, M. R., and Van Meijgaard, E.: Improved representation of East Antarctic surface mass balance in a regional atmospheric climate model, *J. Glaciol.*, 60, 761–770, <https://doi.org/10.3189/2014JoG14J051>, 2014.

Vermote, E. F., Tanré, D., Deuze, J. L., Herman, M., and Morcette, J.-J.: Second simulation of the satellite signal in the solar spectrum, 6S: An overview, *IEEE Trans. Geosci. Remote Sens.*, 35, 675–686, <https://doi.org/10.1109/36.581987>, 1997.

760 Vittuari, L., Vincent, C., Frezzotti, M., Mancini, F., Gandolfi, S., Bitelli, G., and Capra, A.: Space geodesy as a tool for measuring ice surface velocity in the Dome C region and along the ITASE traverse, *Ann. Glaciol.*, 39, 402–408, <https://doi.org/10.3189/172756404781814627>, 2004.

Warren, S. G.: Optical properties of snow, *Rev. Geophys.*, 20, 67–89, <https://doi.org/10.1029/RG020i001p00067>, 1982.

Watanabe, O.: Distribution of surface features of snow cover in Mizuho Plateau, <http://id.nii.ac.jp/1291/00000854/>, 1978.

765 Wendler, G., André, J. C., Pettré, P., Gosink, J., and Parish, T.: Katabatic winds in Adélie coast, *Antarct. Meteorol. Climatol. Stud. Based Autom. Weather Stn.*, 61, 23–46, <https://doi.org/10.1029/AR061p0023>, 1993.

Zanter, K.: Landsat 8 (L8) data users handbook, *Landsat Sci. Off. Website*, 2019.

770 Appendix A

Sensor	Tile	Scene	Solar Zenith (deg)	Azimuth (deg)
OLI	069119	25-Nov-2013	69	89

OLI	069119	11-Dec-2013	67	91
OLI	069119	27-Dec-2013	67	93
OLI	069119	28-Jan-2014	72	95
OLI	069119	28-Nov-2014	68	89
OLI	069119	17-Dec-2015	67	92
OLI	069119	18-Jan-2016	70	95
OLI	069119	04-Nov-2017	74	87
OLI	069119	10-Nov-2019	72	88
OLI	069119	28-Dec-2019	67	93
OLI	069119	29-Jan-2020	73	95
OLI	081114	31-Oct-2014	68	62
OLI	081114	02-Dec-2014	61	65
OLI	081114	18-Dec-2014	60	67
OLI	081114	06-Jan-2016	62	69
OLI	081114	30-Nov-2019	62	65
OLI	081114	17-Jan-2020	64	70
S2	T51CWL	10-Jan-2018	67	87
S2	T51CWL	02-Jan-2021	66	84
S2	T52CEA	13-Dec-2016	59	59
S2	T52CEA	27-Dec-2020	59	61

Table A1. Landsat (OLI) and Sentinel-2 (S2) images in the EAIIST (069119 and T51CWL tiles for L8OLI and S2, respectively) and It-ITASE (081114 and T52CEA tiles for L8OLI and S2, respectively) areas used in the study with corresponding Solar Zenith and Azimuth angles from the Landsat/Sentinel Metadata.

Year	It-ITASE		EAIIST	
	Nº of stripes	Percentage of the total	Nº of stripes	Percentage of the total
2008	5	0.4 %	5	0.5 %
2009	13	0.9 %	11	1.2 %
2010	27	1.9 %	27	2.9 %

Tabella formattata

2011	128	9.0 %	44	4.7 %
2012	27	1.9 %	16	1.7 %
2013	110	7.7 %	89	9.5 %
2014	217	15.2 %	184	19.6 %
2015	136	9.5 %	61	6.5 %
2016	593	41.6 %	398	42.5 %
2017	169	11.9 %	102	10.9 %

Table A2. Frequency of REMA DEM stripes at the EAIIST and It-ITASE sites from different years, based on the REMA strip index.

EAIIST		It-ITASE					
Dataset	Average	Max	Min	Dataset	Average	Max	Min
<i>Landsat 8</i>	224°	232°	212°	<i>Landsat 8</i>	240°	250°	215°
<i>ERA5</i> ≥ 0 m/s	225°	230°	220°	<i>ERA5</i> ≥ 0 m/s	227°	236°	215°
<i>ERA5</i> ≥ 3 m/s	225°	229°	220°	<i>ERA5</i> ≥ 3 m/s	226°	233°	217°
<i>ERA5</i> ≥ 5 m/s	225°	229°	220°	<i>ERA5</i> ≥ 5 m/s	226°	234°	217°
<i>ERA5</i> ≥ 7 m/s	225°	235°	220°	<i>ERA5</i> ≥ 7 m/s	227°	236°	218°
<i>ERA5</i> ≥ 11 m/s	223°	229°	216°	<i>ERA5</i> ≥ 11 m/s	231°	240°	223°

780 Table A3. Wind direction statistics (average, maximum and minimum values) for the considered datasets: Landsat 8 at 30 m spatial resolution and ERA5 at 30 km spatial resolution (divided into 5 sub-datasets according to wind speed) at the EAIIST and It-ITASE sites.